Science
AAAS

Supplementary Materials for
Millennial storage of near-Moho magma

Euan J. F. Mutch, John Maclennan, Tim J. B. Holland & Iris Buisman

Correspondence to: ejfm2@cam.ac.uk, em0242@my.bristol.ac.uk.

This PDF file includes:

Materials and Methods

Analytical Methods

Ultramafic cumulate nodules were picked from hand-crushed glassy tephra collected from the Borgarhraun eruption crater ($65.830°$ N $16.881°$ W) in 2009 and 2014. The nodules were then mounted in epoxy 1-inch rounds and polished using silicon carbide papers and Metprep diamond suspension down to $0.25\,\mu\mathrm{m}$ grade.

QEMSCAN and EDS

The mineralogy and compositional variability across 25 nodule fragments was assessed using QEMSCAN (Quantitative Elemental Mapping SCANning) maps collected using two Bruker XFlash 6|30 Energy Dispersive Spectrometers on a FEI Quanta 650FEG SEM at the University of Cambridge. The QEMSCAN system includes an automated spectrum acquisition and classification procedure. Analyses were performed by obtaining field-scans, providing a complete characterisation of particle surfaces above a predefined electron backscatter threshold. The brightness coefficients were calibrated against quartz, gold and copper. Spectra were collected at 25 kV and 10 nA with 2000 total X-ray counts at a $2\,\mu\mathrm{m}$ spacing, and compared to a Species Identification Protocol (SIP) that discriminate minerals on the basis of their characteristic X-ray and electron backscatter intensities. Custom SIP lists with optimised compositional ranges for each individual mineral phase were used to produce elemental maps that could be used to interrogate compositional zoning. Al and Cr EDS (energy dispersive X-ray spectroscopy) maps were used to evaluate compositional variability and zoning in spinel inclusions in the nodules.

EPMA

Compositional zoning in the spinel crystals was quantified by electron probe microanalysis (wavelength dispersive X-ray spectroscopy, EPMA) using a Cameca SX100 with 5 wavelength dispersive spectrometers at the University of Cambridge. Profiles were measured across 7 spinel crystals that were large enough to retain some zoning characteristics. Calibration was carried out using a mixture of natural and synthetic minerals and oxides. Instrument drift and measurement uncertainty was assessed by measuring olivine and clinopyroxene secondary standards. An accelerating voltage of 15 kV was applied with a working current of 40 nA for all elements. On peak count times of 20 s were used for Si; 30 s for Mg, Fe, Al and Cr; 50-60 s for Ni, Zn, and Mn; and 90 s for Ti. Half count times were used off peak. A spot size of $1\,\mu\mathrm{m}$ was selected, with a typical profile point spacing of $3\,\mu\mathrm{m}$. This was to ensure high spatial resolution and limit any potential convolution between adjacent interaction volumes. Profiles were measured from the edge of the crystal into the interior. Efforts were made to avoid melt inclusions, which inhibited measuring edge-to-edge profiles. Spinel mineral formulae were calculated from the EPMA data relative to 4 oxygens and ferric iron (Fe^{3+}) was calculated stoichiometrically. Cr# was calculated using Cr and Al atoms per formula unit (apfu).

Interstitial melt pockets adjacent to coarse spinel crystals and the matrix glass were also measured using EPMA. A defocussed beam of $5\,\mu m$ was used to limit alkali migration (*33*). An accelerating voltage of 15 kV was applied with a working current of 6 nA for all elements. Elements measured (with count times in seconds in brackets) were: Na (10), Ca (40), Ti (60), K (10), P (60), Si (20), Mg (80), Al (80), Fe (20), Cr (80), Mn (80), Ni (100). Melt pockets adjacent to the spinels have a composition that is different to that of the carrier liquid, which is shown in Fig. S6.

Plagioclase profiles were measured with an accelerating voltage of 15 kV and a working current of 10 nA for major (Ca, Al, Si, Na) and minor elements (Mg, Ti, K, Fe). On peak count times of 20 s were used for major elements and 90-110 s for minor and trace elements, with half count times off peak. For both sets of analyses, a spot size of $1\,\mu m$ was selected, with profile point spacing varying from $5\,\mu m$ (typically within $150\,\mu m$ of the crystal edge) and $20\,\mu m$ (distances exceeding $150\,\mu m$ from the edge).

SIMS

Plagioclase compositional data were collected using a Cameca 1270 Secondary Ion Mass Spectrometer (SIMS) at the Edinburgh Materials and Micro-Analysis Centre (EMMAC), University of Edinburgh. Spot analyses were made with a 3 nA $^{16}O^-$ primary beam of 22 keV net impact energy focussed to approximately $15\,\mu m$. This generated 10 keV positive secondary ions with 75 eV energy filtering (100 eV window). Spots were individually placed across crystals from rim to core. A $60\,\mu m$ image field was apertured to give a $20\,\mu m$ collection window. Isotopes measured by coarse spot analysis include (count times in seconds are in brackets): ^{30}Si (2), ^{26}Mg (5), ^{42}Ca (2), ^{47}Ti (5), ^{88}Sr (5), ^{138}Ba (5), ^{39}K (5), ^{7}Li (5), ^{89}Y (5), ^{140}Ce (5), ^{139}La (5) and ^{85}Rb (5). Analyses were averaged over 10 cycles. ^{30}Si (2), ^{26}Mg (5), ^{47}Ti (5), ^{88}Sr (5), ^{7}Li (5), ^{39}K (5), ^{42}Ca (2) and ^{138}Ba (5) were routinely measured using high resolution step scan analyses. Step scans were collected by initially setting a line scan pre-sputter of 3.2 nA using $10\,\mu m$ steps. Analyses were made with a $2.5\text{x}10^{-11}$ A primary beam focussed to approximately $2\,\mu m$, with step sizes also being set to $2\,\mu m$. Analyses were averaged over 3 cycles. There was no energy offset and a 100 eV energy window was used. There were no losses due to field apertures as the spot was much smaller than collection window. The scan position in the centre of the line was positioned with scanning ion imaging of Na and Si. Electron multiplier ions counting was used and all data were dead-time corrected (51 ns dead time). An entrance slit of $100\,\mu m$ and exit slit of $400\,\mu m$ were used. The nominal mass resolution was about M/ΔM 2400. The SIMS data was then normalised relative to Si measured by EPMA. Step scan data was normalised to coarse SIMS spots in order to convert from raw counts into concentrations. Compositional profiles measured across Borgarhraun plagioclases are shown in Fig. S21-S31.

Image calibration

Al and Cr (apfu) EPMA profiles were used to calibrate the greyscale intensity of Al and Cr EDS maps collected for each nodule, which were then combined to create Cr# maps. The core compositions and average widths of all spinel crystals from selected nodules were sampled from the Cr# maps using ImageJ image processing software (*34*). This allowed the relationship between core composition and crystal width to be assessed in a consistent way, and thus evaluate the role of diffusive processes. The image calibration reproduces calculated Cr# from EPMA profiles with an average deviation of 0.0046. The calibration and its associated performance can be seen in Fig. S33 and Fig. S34.

Thermodynamic Modelling

Equilibrium thermodynamic modelling using THERMOCALC and the new melt model of Holland et al. (*35*) was applied to bulk compositions typical of the wehrlitic nodules in order to estimate the P-T conditions that could accompany the observed Cr# zoning in the measured spinels.

The solid bulk composition was kept constant at 5% spinel, 35% clinopyroxene and 60% olivine, using measured wehrlite mineral compositions. Increasing quantities (5-40%) of Borgarhraun glass composition (*36*) were added to the bulk to model an interstitial liquid phase. Pressure in the calculations was maintained at 0.8 GPa (8 kbar), and temperature was varied from $1300\,^{\circ}\mathrm{C}$ down to the solidus for each composition. Only the model with 20% added melt matches the observed range in spinel compositions. It reaches near-solidus conditions at approximately $1215\,^{\circ}\mathrm{C}$, the temperature used in the diffusion modelling (Fig. S3). In this scenario the bulk of cooling and crystallisation is expected to take place soon after emplacement (< 1 year) and diffusive re-equilibration effectively starts once cooling has completed (*37*). Phase compositions and modal abundances from the thermodynamic models are shown in Fig. S4.

Diffusion Modelling

The temperature of the mush pile ($1215 \pm 30\,^{\circ}\mathrm{C}$) was estimated using THERMOCALC (see above); pressure (0.8 ± 0.14 GPa) was estimated using both clinopyroxene-liquid (*12, 13*) and OPAM (olivine-plagioclase-augite-melt) barometry (*18, 38*). A Fe^{3+}/Fe_{total} value of 0.14 ± 0.02, typical of depleted Icelandic basalts (*26*), was used. Oxygen fugacity (fO_2) was calculated from the Sigurdsson et al. (*36*) glass composition and Fe^{3+}/Fe_{total} using equation 7 of Kress and Carmichael (*39*). Calculated oxygen fugacities had a typical $\log fO_2$ of ΔFMQ + 0.14. The a_{SiO_2} of the Borgarhraun magma (0.62 ± 0.03) was calculated using rhyolite-MELTSv1.0.2 (*40, 41*) using the liquid's affinity for quartz of measured tephra glass compositions (*36*).

The diffusivity of Cr-Al exchange in Cr-spinels was defined here using a new multivariate regression (equation 1) through the spinel diffusion experiments of Suzuki et al. (*24*) and the cut gem experiments of Posner et al. (*25*). The gem-gravel experiments of Posner et al. (*25*)

were excluded from the regression as it is postulated that their elevated Ta content may impose extraneous vacancies that would facilitate enhanced Cr diffusion. The uncertainty structure associated with this equation is taken into account and is expressed in the form of a covariance matrix between all of the parameters associated with the diffusion coefficient (Table S2).

$$\ln D_{\mathrm{CrAl}} = a + b \ln f\mathrm{O}_2 + h\mathrm{Cr}\# + \frac{q + vP}{T} + jP \tag{1}$$

where a, b, h, q, j and v are the regression parameters presented in Supplementary tables S1 and S2. P is pressure (Pa), T is temperature (K), $f\mathrm{O}_2$ is oxygen fugacity and Cr# is chrome number. The regression typically recovers all of the experimental data within 1-2 ln units (0.5-0.9 $\log_{10}$ units) (Fig. S7). Regressed diffusion coefficients are typically a factor of 2 greater than those from the Suzuki et al. (*24*) equation due to some inaccuracies in extracting the Suzuki et al. (*24*) data graphically. Regression statistics can be seen in Supplementary file D4. The Suzuki et al. (*24*) data were collected at temperatures of 1400-1700 °C, pressures of 3-7 GPa, Cr# of 0-0.8 and $f\mathrm{O}_2$ was between the wüstite-magnetite (WM) and iron-wüstite (IW) oxygen buffers. The Posner et al. (*25*) data were collected at temperatures of 975-1200 °C, a pressure of 1 bar, a Cr# of 0, and $f\mathrm{O}_2$ was between WM-2 and WM+2. Due to the dearth of experimental data, considerable extrapolation outside the experimental conditions is needed for the regression of this study to be applied to Borgarhraun. The experimental work by Posner et al. (*25*) suggests a separate diffusion mechanism may operate at lower temperature for Cr tracer diffusion (shown by differences in slope in Fig. S8). In this instance, the Cr-Al interdiffusion coefficients of Suzuki et al. (*24*) measured in Cr poor spinels are equivalent to Cr tracer diffusion coefficients. The regression of this study merges both diffusion mechanisms, but is dominantly weighted by the Suzuki et al. (*24*) data. Linear extrapolation of the diffusion mechanisms of Suzuki et al. (*24*) and Posner et al. (*25*) show that they intercept close to the temperature of the Borgarhraun mush (Fig. S8). This means the offset between these two different mechanisms is reduced and will minimise the error in timescale estimates that result from the wrong choice of diffusion mechanism. Therefore, the regression of this study, which closely follows the Suzuki et al. (*24*) mechanism, is acceptable in this instance and incorporated in the uncertainties. The uncertainties arising from temperature variations are likely to be overstated in this study due to the higher temperature dependence (i.e. a higher activation energy) of the Suzuki et al. (*24*) mechanism. Pressure dependence is small, so extrapolation to lower pressures is reasonable (*24*). Extrapolation is also applied in terms of $f\mathrm{O}_2$ conditions as most experimental data have been collected close to the wüstite-magnetite (WM) oxygen buffer, whilst the Borgarhraun magma is close to FMQ + 0.14. Two experiments from Posner et al. (*25*), which have been included in the regression, were conducted at WM + 2, which is very close to FMQ at 1100 °C. Greater vacancy concentrations associated with Fe^{3+} may cause $D_{\text{Cr-Al}}$ to increase, and may be associated with a different diffusion mechanism. Until more experiments are conducted at higher $f\mathrm{O}_2$ conditions, the combination of Suzuki et al. (*24*) and Posner et al. (*25*) experiments provide the best approximation for Cr-Al interdiffusion in spinels.

3D and 2D finite element diffusion models using FEniCS (*22*) for Cr-Al interdiffusion were

conducted as part of this study. Each diffusion model used a Crank-Nicholson time-stepping scheme (*42*) and linear finite elements were used to represent elemental concentrations. The number of time steps was kept constant at 300 per model/realisation. As the diffusivity of Cr-Al exchange is compositionally dependent, a spatially dependent version of Fick's Second Law was used in the modelling (equation 2).

$$\frac{\partial C}{\partial t} = \nabla \left(D(C) \nabla C \right) \tag{2}$$

where t is time and C is the concentration of the diffusing species. $C = C_0$ on the boundary (Dirichlet boundary conditions).

As the compositionally dependent term in the diffusion coefficient is also the species that is diffusing (i.e. Cr#), the problem was treated as being non-linear and was solved using a Newton solver at each time step. Spinel is a cubic mineral, therefore diffusive anisotropy did not need to be considered. It is assumed the melt pockets that surrounded the spinels for most of their history acted as a buffered reservoir in which the elements of interest could diffuse into. Given that there are only 2D sections of fragments of the crystal mush, it is difficult to properly constrain the full geometry and size of the melt network. Dirichlet boundary conditions (i.e. fixed at a constant value) were therefore maintained at the crystal edges. As the growth history of these spinels cannot be constrained by profiles of slower diffusing elements, diffusion from homogeneous core compositions (i.e. constant initial conditions) was assumed which are associated with maximum diffusively-controlled residence times. All crystals were assumed to have the same initial core Cr# of 0.41 as determined by the largest measurable spinel, which is most likely to retain its original core composition. These core compositions also correspond with spinel Cr# calculated for some of the highest temperatures using THERMOCALC.

2D diffusion models were combined with a nested sampling Bayesian inversion scheme using the MultiNest algorithm (*23, 43*) and the Python wrapper PyMultiNest (*44*), in order to invert for magma residence time by fitting the measured Cr# profile data. Outlines of spinel crystals were traced in ImageJ (*34*) and were converted into 2D planar finite element meshes using Gmsh software (*45*). Mesh resolution was set to 25, however the mesh was refined approximately $100\,\mu\mathrm{m}$ from the edge of the crystal, where the majority of diffusion was expected to take place. This typically produced meshes with 20,000 vertices and ensured a compromise between computing time and mesh resolution. During each realisation of the Bayesian inversion, the mesh remained the same in spite of any changes to the size of the time step. This would mean that the numerical stability of the solution could be compromised in realisations where the Courant-Friedrichs-Lewy (CFL) condition is exceeded. This would only occur when the model is first initialised and usually stabilised once the target time has been reached. At the end of each realisation, the 2D mesh was sampled along a 1D profile where the EPMA data was collected.

A log uniform prior was used for time (0-10,000 years). Independent Gaussian prior distributions, set with 1σ uncertainties, were used for intensive parameters including: temperature (T), pressure (P), and ferric iron content of the system (Fe^{3+} /Fe_{total}). Multivariate Gaussian

prior distributions were used for coefficients in the diffusion equations which were controlled by their respective covariance matrices. The variation in T, P and Fe^{3+} /Fe_{total} for each of the runs are also shown in Fig. S9. The log likelihood function of the inversion employed a χ^2 misfit between the model and the measured observations along the profile which were weighted by their analytical uncertainties. The MultiNest algorithm employed ellipsoidal nested sampling (*23, 43, 44*). A fixed size of parameter vectors or "live points" (n = 400) were drawn randomly from the prior distributions and were clustered into multi-dimensional ellipses. New points were selected from the prior within this ellipsoid until one was obtained with a likelihood that was greater than the lowest likelihood point which was then removed (*23,43,44*). The selection of diffusion coefficient prior points using the derived covariance matrices reduced the size of the parameter space explored and thus reduced uncertainty. The algorithm terminated once convergence of the marginal likelihood was attained. Model fits and temperature-time posterior distributions for each of the modelled profiles are shown in Fig. S10-S12. The posterior distributions of the intensive parameters for each modelled spinel crystal are shown in Fig. S13-S19.

3D spherical spinel diffusion modelling

A series of forward 3D models using a spherical geometry were used to assess the impact of crystal radius on spinel core composition. Spherical meshes with different radii were generated using mshr from the CGAL library (*46*). In each case the mesh resolution was set to 30, which typically corresponds to 10,000 vertices. Homogeneous initial conditions were used with the core Cr# of the largest spinel. Dirichlet boundary conditions (fixed boundary conditions) were set at the edges with the average rim composition of the spinels found in each nodule. Each spherical mesh was used in a forward model that was run for different end times. The composition of the centre of the sphere was then sampled and taken to be the core composition. Models were conducted using the estimated temperature of the mush pile ($1215\,^{\circ}\mathrm{C}$). In all cases a homogeneous spinel with a Cr# of 0.41 was used as an initial condition. The results of these models are shown in Fig. 1 and Fig. S1.

Plagioclase 3D bulk diffusion models

Plagioclase macrocrysts were picked from the same tephra as the wehrlite nodules. This phase was particularly rare, accounting for less than 1 % of the volume of crushed tephra. Macrocrysts range in size from $500\,\mu\mathrm{m}$ up to $2400\,\mu\mathrm{m}$ width. There is some compositional diversity in the plagioclase crystal population, however most crystals have been interpreted to have co-crystallised with forsteritic olivine (*47*). From the plagioclases picked as part of this study, we identified at least three distinct crystal populations based on texture and zoning pattern. The first consists of coarse tabular crystals with high-anorthite cores (An_{86-90}) surrounded by sharp lower-anorthite rims (An_{80}). The cores often have rounded edges; either the result of textural maturation or resorption. They also appear to be relatively homogeneous with few in-

ternal zones. The number and texture of melt inclusions does vary from few prominent melt inclusions, to partially developed sieve textures and large elongated inclusions up to $400\,\mu m$ in length. Some of these crystals are part of glomerocrysts with primitive olivines. It is this population that was the focus of microanalysis and diffusion modelling. The second population have rounded high-anorthite cores and no rims and appear to have undergone resorption during entrainment into the carrier liquid and transport to the surface. Some of these crystals show further evidence of resorption with prominent embayments. The third population consists of smaller, higher aspect ratio plagioclase crystals that are intergrown with clinopyroxene in nodules.

Trace elements from measured Borgarhraun plagioclase macrocrysts appear to display different levels of intercrystalline and intracrystalline equilibria (Fig. S20). Most plagioclase macrocrysts with rims, which were analysed using SIMS, appear to have reached pseudo-equilibrium for Mg at mush conditions that are either colder or with a more MgO-poor liquid than the carrier liquid as defined by the low-anorthite rims. Slower diffusing elements, such as Sr and Ba, display considerably more scatter in their core compositions. This could be due to the larger uncertainties associated with these elements given their relative changes across each crystal are much smaller ($\sim$ 25 ppm for Sr and $\sim$ 1 ppm for Ba) which is approaching the lower limits of SIMS precision. Alternatively, this pattern may represent disequilibria for these elements where the cores of these macrocrysts have grown from melts with varying degrees of trace element enrichment. The degree of disequilibrium was difficult to assess given uncertainties and biases associated with the experimental partitioning relationships (*48*) and the uncertainties within the analyses themselves.

Bulk 3D spherical diffusion models were performed to assess the timescales of equilibration of high-anorthite cores. Forward models were conducted to assess the equilibration timescale of the largest high-anorthite plagioclase core ($1200\,\mu m$) using Mg, Sr and Ba diffusion. Models were conducted using the estimated temperature of the mush pile ($1215\,^{\circ}C$) and the a_{SiO_2} estimated for Borgarhraun melt compositions (0.62). Diffusion of Mg in plagioclase was modelled using an equation that combines the experimental data of Faak et al. (*49*) and Van Orman et al. (*50*). This allowed for the a_{SiO_2} to be accounted for when calculating D_{Mg}. Sr was modelled using the diffusion equations of Cherniak et al. (*51*) and Giletti et al. (*52*). Ba was modelled using the diffusion equation of Cherniak (*53*). Given that the diffusive anisotropy of the modelled trace-elements in plagioclase is relatively minor ($<$ 2-3 times), diffusion was treated as being isotropic (*49–53*). Plagioclase cores were assumed to be homogeneous in terms of their anorthite content (An_{90}). This simplified the diffusion equation that needed to be used as fluxes relating to chemical potential gradients from variations in anorthite content did not need to be considered. Homogeneous initial conditions were used for each element. For Mg, initial conditions were calculated with a PETROLOG (*54*) reverse crystallisation model using the measured tephra glass as a starting composition. Pressure and fO_2 were fixed at 0.8 GPa and ΔNNO - 0.7. The temperature ($1280\,^{\circ}C$) and MgO of the melt (10.7 wt.%) that corresponded to growth of high-anorthite plagioclase ($An_{>84}$) was used to calculate the initial plagioclase Mg composition. This corresponded to a core composition of 1548 ppm. For Sr and Ba, the high-

est core concentration measured (165 ppm for Sr and 3.4 ppm for Ba) was used as the starting composition. This only accounted for diffusive equilibration of crystals that grew from enriched melts, but still gave a typical time of equilibration of the coarsest component of the plagioclase crystal cargo. A Dirichlet boundary condition (fixed boundary condition) at the edge was set at the current measured core composition adjacent to the lower An rims for each element. For Mg this was 1200 ppm, Sr was 140 ppm and Ba was 2.4 ppm. The composition of the centre of the sphere was tracked throughout the forward model to assess its modification by diffusion.

3D spherical models with different crystal radii were also run to assess the equilibration time for crystal cores of different sizes. Here, the same initial conditions were used, however the forward models were run until the time in which the centre composition initially matched the edge composition accounting for the analytical uncertainty (standard errors) from SIMS analyses (10 ppm for Mg, 1 ppm for Sr, and 0.1 ppm for Ba). This timescale was then recorded as the equilibration timescale. The results of 3D Plagioclase diffusion modelling are in Fig. S32. 3D spherical diffusion models for Mg suggest equilibration would take place after only 570 years at temperatures of $1215\,^{\circ}\mathrm{C}$, providing a minimum estimate of residence times. Core disequilibria for Sr and Ba in some of the larger plagioclase crystals support our assertion of residence times of hundreds to thousands of years as full equilibration of a $1200\,\mu\mathrm{m}$ radius sphere would require 3100 years for Sr and approximately 26,000 years for Ba.

Given that the anorthite content in these crystal cores varies by only 4 An units, the assumption of a homogeneous core (An_{90}) was justified. Any changes in diffusivity associated with anorthite content were minor. For example, D_{Mg} for An_{86} is only 25 % faster than for An_{90} (*49, 50*).

Although not ideal, the 3D spherical approximation we use to estimate the equilibration timescales of trace elements in the plagioclase cores is still better suited than 1D planar approximations that provide no account of diffusion from multiple dimensions. The plagioclases that were measured had relatively low aspect ratios, possibly related to slow cooling and textural maturation (*55*). This was better suited for 3D spherical approximations than high aspect ratio plagioclases that formed by rapid cooling (*55*). 1D planar approximations would overestimate the timescales of equilibration. Modelling with a 3D tabular geometry would reduce the timescales of equilibration, meaning our spherical approximations are also an overestimates. As the equilibration timescales provide upper and lower limits on storage timescales, changing the geometry to tabular would shift these limits around the spinel timescales. These plagioclase timescales should therefore be treated as a supporting constraint to the spinel timescales which have proper textural context.

Diffusive re-equilibration of spinel crystals in a mush environment

Crystallisation of the spinels and the surrounding clinopyroxene is expected to take place rapidly after magma emplacement, within 1 year, as the timescales of mixing and crystallisation in a convecting sill appear to be similar (*17, 37*). Chains of spinels observed within some nodules (Fig S1c, Fig S1g) could also support rapid crystallisation given that corner growth and chain

formation have been suggested to be favoured by high degrees of supersaturation (*56*). Alternatively, these spinel chains may have been formed by synnuesis.

Thermodynamic modelling of the variation in spinel composition indicates that the difference in composition between the highest Cr# spinel cores and the low Cr# rims can be accounted for by re-equilibration over a cooling interval of around $75\,^{\circ}\mathrm{C}$ (see thermodynamic modelling section), similar to the cooling interval previously inferred for crystallisation of the Borgarhraun olivines (1350-$1220\,^{\circ}\mathrm{C}$) (*18,57*). The spinels were initially encased at high temperature and subsequently equilibrated with the surrounding melt pockets and grain boundary films following cooling to lower temperature (Fig. S5). The spinels have retained their equidimensional forms and appear to have undergone very little deformation, which precludes stress-directed lattice diffusion of Cr and Al to create the concentric zoning patterns that are observed (*19*).

The geometry, extent and the interconnectivity of the melt network cannot be properly resolved from just 2D sections of the nodules. However, melt pockets and liquid films like those shown in Fig. S6 have been suggested to play an important role in the final stages of crystallisation of large mafic intrusions (*14*). Interconnected late-stage grain boundary liquid films at low liquid fractions have been invoked as a way of explaining apatite compositions in gabbroic cumulates (*14, 20*), therefore a permeable low liquid fraction melt network may have been sustained for a long period of time. The melt networks may also have been more extensive than currently observed, given the important role of the liquid in mush homogenisation (*21*). They may have since been obscured by additional crystallisation of interstitial clinopyroxene, which is the dominant phase to crystallise in the nodules over the cooling interval (Fig. S4). Further, the interstitial melt networks may not have been ubiquitous with different spinel crystals potentially being sealed off by the enclosing clinopyroxene at different times. This is observed in the case of BORG_NOD1_N3_SP1_P1 (Fig. S11a), where the rim composition on the face of this crystal (which is no longer next to a melt lens) only extends to a Cr# of 0.37 whereas the rest of the crystal in contact with the melt pockets has a much lower Cr# of 0.34 (see Fig. S1a and Fig. S6a). This profile returned a shorter diffusion timescale of approximately 900 years, which could mark the time at which the crystal face got enclosed by clinopyroxene. Diffusion around the rest of the crystal continued to act preferentially on the faces in contact with the melt lenses and melt pockets. Many of the smaller, homogeneous spinels may have been completely equilibrated (which would require approximately 500 years according to Fig. 1) before they lose any connection with the melt network. We therefore argue that the melt network was ubiquitous at one point, but was gradually being lost by clinopyroxene crystallisation.

The composition of the melt pockets adjacent to the spinel crystals are different to that of the final carrier liquid (Fig. S6), which suggests that these melt networks were isolated from the open magma body. The fact that the trace element composition of olivine-hosted melt inclusions converges towards the carrier liquid composition with more evolved olivine hosts suggests that the crystal cargo and carrier liquid are related to the initial distribution of primary melts (*11, 18*). Therefore, the difference in melt compositions cannot be due to the emplacement of an unrelated carrier liquid. The elevation in Cr content of the interstitial liquid could be accounted for by the flux of Cr out of the spinels. The variability in spinel Cr# between different nodules highlights

heterogeneity within the mush and the development of micro-environments in which the spinels equilibrated with.

The results of this study show that following emplacement and initial crystallisation, primary basaltic mushes can be stored in the lower crust for hundreds to thousands of years. The poikilitic texture, where clinopyroxene oikocrysts surround olivine chadacrysts, that makes up a fundamental part of the Borgarhraun wehrlitic nodules is a common feature observed in many mafic plutonic rocks, such as the intrusive suite on the Isle of Rum, Scotland (*58–60*) and lower crustal gabbros sampled directly from oceanic sections, such as Hess Deep (*15, 61*) or from ophiolites (*16*). As the Cr# of the spinels changes in response to exchange with the adjacent melt pockets following cooling and enclosure by the clinopyroxene, the diffusive zoning patterns that is observed can be used as a chronometer for the development of this distinctive texture.

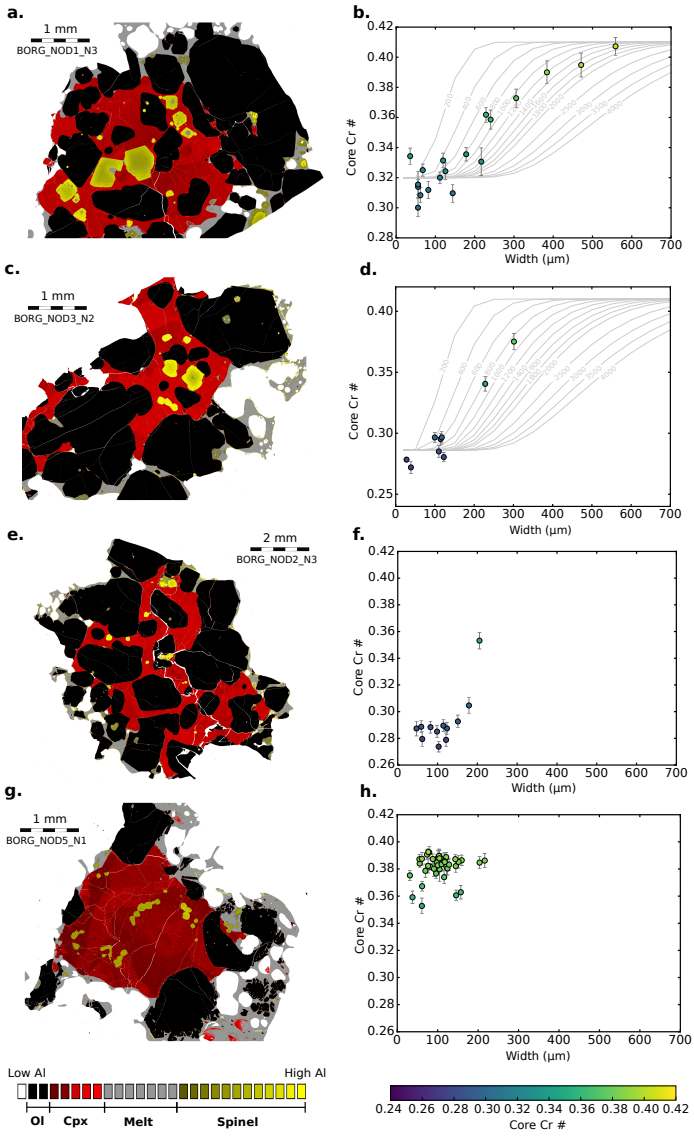

Fig. S1: Al maps collected by energy dispersive spectroscopy (EDS) of Borgarhraun wehrlitic nodules with poikilitic texture (left), and accompanying plots that show spinel core Cr# compositions with respect to their measured width (right). Samples shown are BORG_NOD1_N3 (**a**, **b**), BORG_NOD3_N2 (**c**, **d**), BORG_NOD2_N3 (**e**, **f**), and BORG_NOD5_N1 (**g**, **h**). Coarser spinel crystals enclosed within the clinopyroxene display prominent zoning in their Al contents (and thus Cr#), whilst the smaller spinel crystals appear to be homogeneous. This is shown in the accompanying plots where clinopyroxene-hosted spinels with widths below $200\,\mu m$ have similar core Cr#, whilst crystals with widths above this threshold show a systematic increase in core composition with measured width. Differences in composition between each nodule reflects mush heterogeneity. The grey curves in **b** and **d** are 3D spherical spinel diffusion models conducted for different crystal radii and diffusion timescales in years, marked on each curve. The models were conducted at $1215\,^{\circ}C$. These features suggest that these zoning patterns are diffusively controlled.

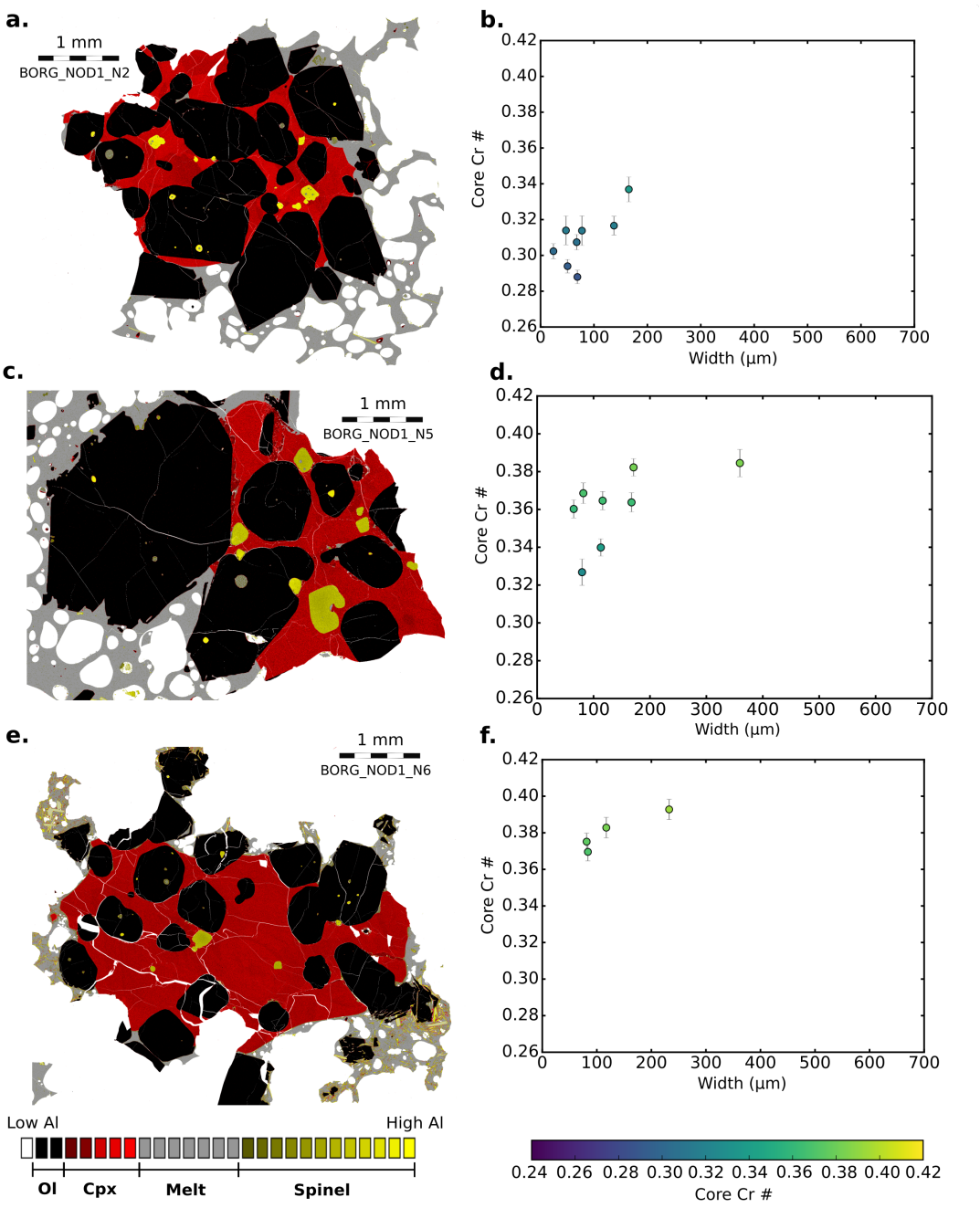

Fig. S2: Al maps collected by energy dispersive spectroscopy (EDS) of Borgarhraun wehrlitic nodules with poikilitic texture (left), and accompanying plots that show spinel core Cr# compositions with respect to their measured width (right). Samples shown are BORG_NOD1_N2 (**a**, **b**), BORG_NOD1_N5 (**c**, **d**), and BORG_NOD1_N6 (**e**, **f**).

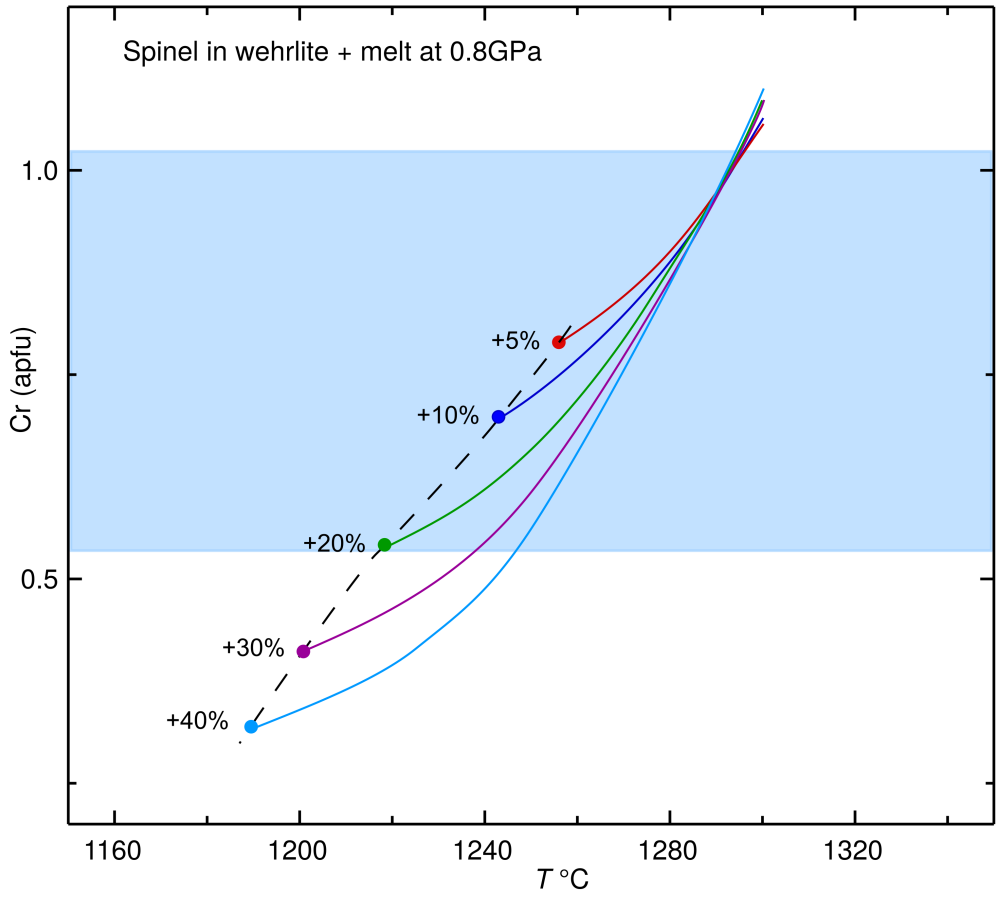

Fig. S3: Calculated Cr contents of spinel, in atoms per formula unit (apfu), as a function of temperature for bulk compositions typical of Borgarhraun wehrlitic nodules (5% spinel, 35% clinopyroxene, 60% olivine). Coloured lines are for different amounts of added Borgarhraun melt on cooling from 1300 °C down to the solidus for each composition (dashed line). The blue region corresponds to Cr contents of observed Borgarhraun spinels. A best cooling interval of 75 °C is inferred from the model with 20% added melt. Calculations were made using THERMOCALC and the new melt model of Holland et al. (*35*).

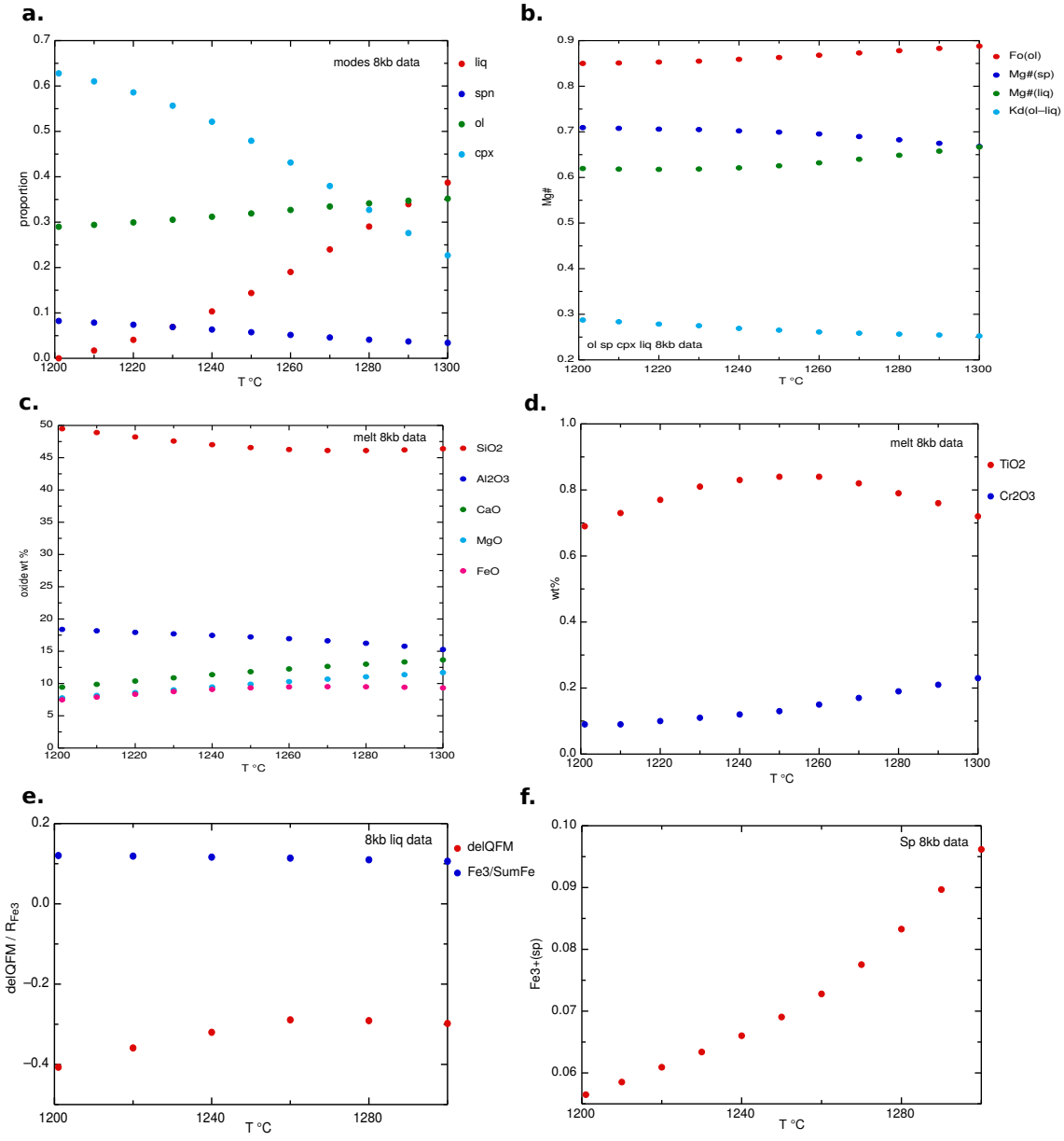

Fig. S4: Results from thermodynamic modelling of Borgarhraun wehrlite nodule bulk composition down the cooling interval discussed in the main text. **a** shows the change in modal abundance of the major phases within the nodules along the cooling interval. **b** shows how Mg# in olivine, spinel and the liquid changes across the cooling interval. The spinel Mg# is predicted to increase marginally as temperature decreases. **c** and **d** show how the composition of the melt changes as the system is cooled. **c** shows major elements and **d** shows minor elements. **e** shows the change in Fe^{3+}/Fe_{total} of the melt and fO_2 of the system. **f** shows the change in Fe^{3+} of the spinels, which decreases with decreasing temperature.

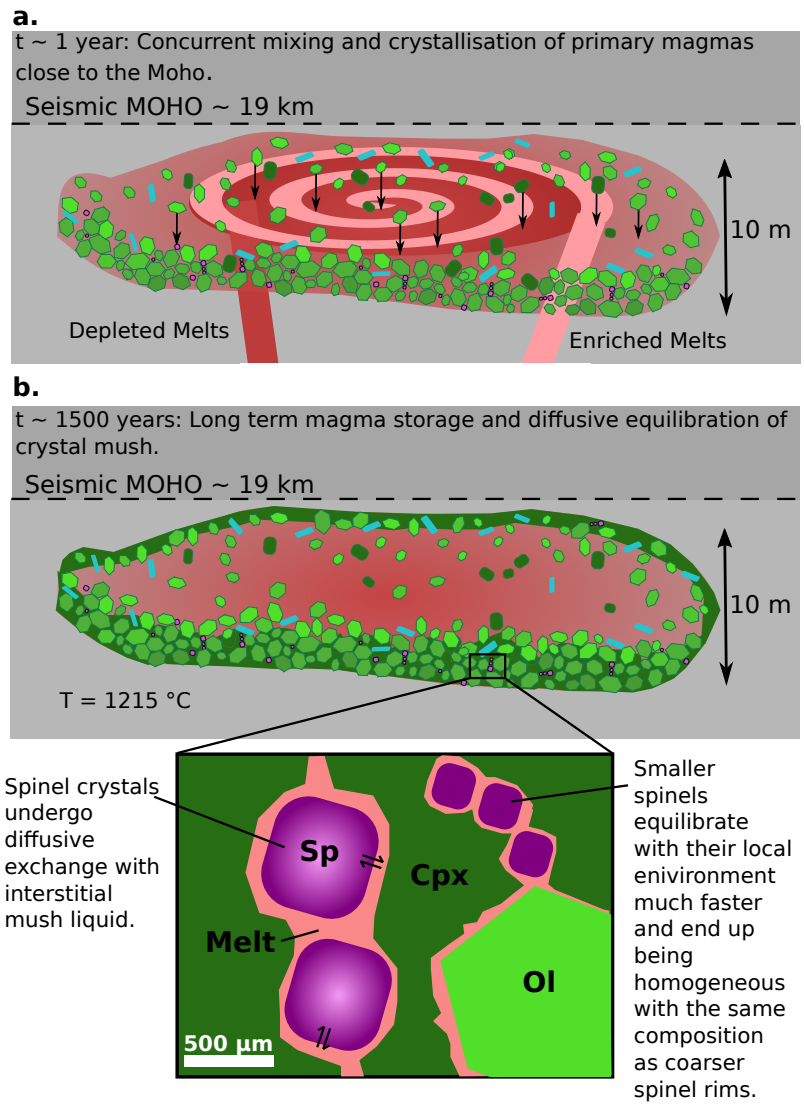

Fig. S5: Schematic cartoon summarising the formation and storage of magmatic mushes that were sampled by the Borgarhraun eruption. **a** shows the concurrent mixing and crystallisation of primary magmas close to the Moho. Mixing and crystallisation are expected to take place over similar timescales (*17,37*), with vigorous convection meaning this process is likely to occur soon after emplacement. Crystallisation takes place over a cooling interval from 1350-1215 °C. Olivine is shown in light green, clinopyroxene in dark green, plagioclase in blue and spinel in purple. **b** shows the long term storage and diffusive equilibration of the crystal mush, which has been estimated to take place over thousands of years. At this point the mush was at a temperature of 1215 °C. Inset is a zoomed in section of the mush showing the diffusive equilibration of spinel crystals with interstitial melt networks. Smaller spinels manage to equilibrate with their local environment much faster.

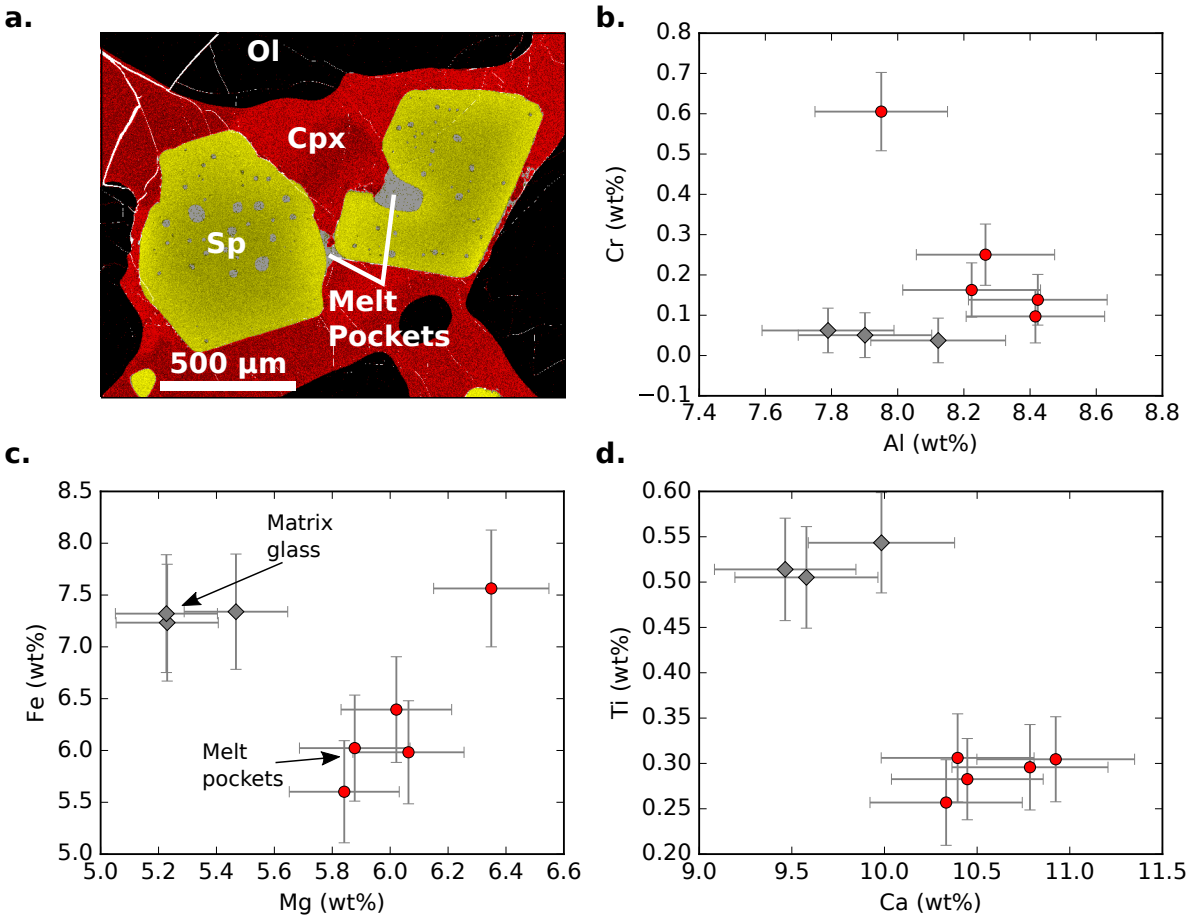

Fig. S6: Wehrlite nodule interstitial melt pocket morphology and composition. **a** is a zoomed in version of an EDS Al map of BORG_NOD1_N3 showing the interstitial melt pockets in contact with the spinel chadacrysts. **b** Al vs. Cr composition of the interstitial melt pockets (red points) and the matrix glass (grey points). **c** Mg vs. Fe glass compositions. **d** Ca vs. Ti glass compositions. The interstitial melt pockets are compositionally distinct to the tephra glass.

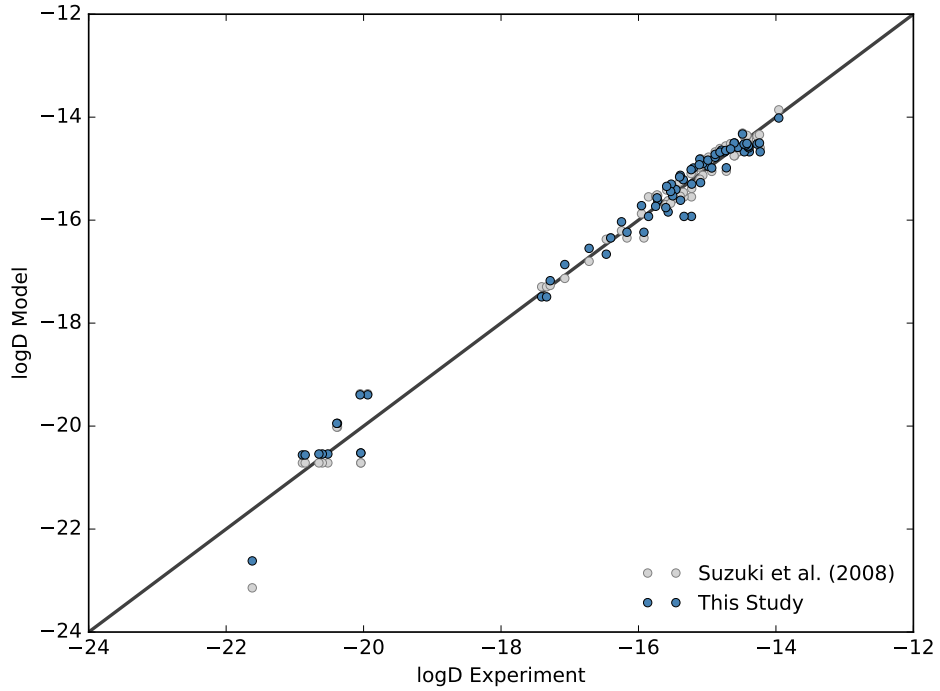

Fig. S7: Plots showing the model predictions of this study's Cr-Al interdiffusion model multivariate regression (blue circles) and that of Suzuki et al. (*24*) (grey circles) when applied to the calibrant experimental database. The regression of this study can retrieve the experimental diffusion coefficients within 0.5 log units, and is similar to the diffusion equation of Suzuki et al. (*24*).

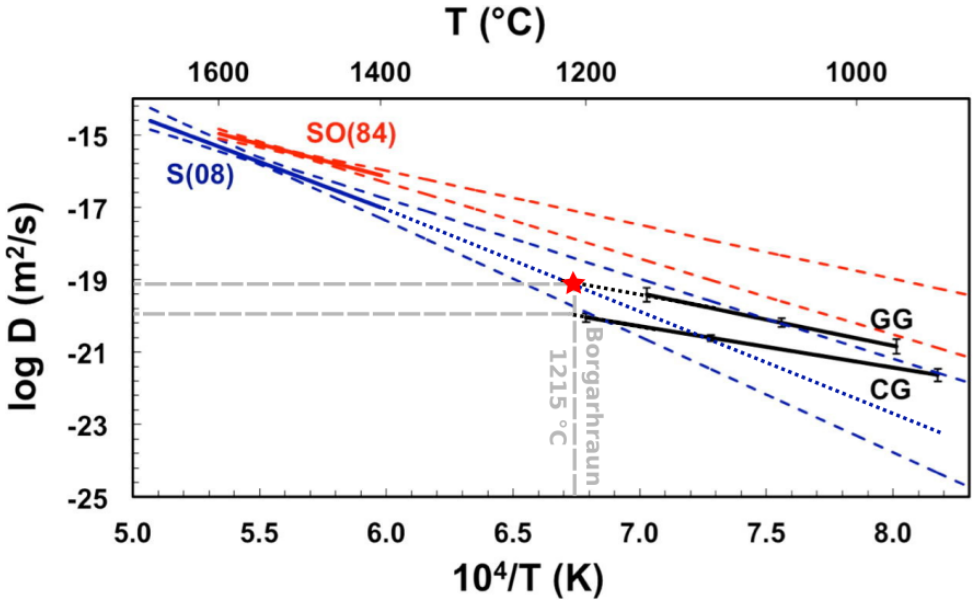

Fig. S8: Comparison of Cr tracer diffusion studies (adapted from Posner et al. (*25*)) relative to the estimated conditions of the Borgarhraun mush (at a temperature of $1215\,^{\circ}\mathrm{C}$ shown by the grey dashed line). The blue line, S(08), is the estimated Cr tracer diffusion coefficient of Suzuki et al. (*24*); the red line, SO(84), is the tracer diffusion coefficient of Stubican and Osenbach 1984 (*62*); and the black lines are from the experiments of Posner et al. (*25*), where GG is the gem gravel experiments and CG is the cut gem experiments. The dashed lines are the 95 % confidence intervals of the experimental studies and the dotted lines are linear extrapolations outside of the experimental conditions. The Cr-Al interdiffusion coefficient regression of this study mostly follows the diffusion mechanism of Suzuki et al. (*24*) meaning that extrapolation to lower temperatures is required. The different slopes of Posner et al. (*25*) suggests that a different mechanism may operate at lower temperatures. The temperature of the Borgarhraun mush is at the point where these two different mechanisms intersect when extrapolated (red star). Therefore using an extrapolation of the Suzuki et al. (*24*) will unlikely cause erroneous timescale estimates. In fact, the calculated uncertainties due to temperatures will likely be much larger than necessary given that the Suzuki et al. (*24*) mechanism has a much greater temperature dependence.

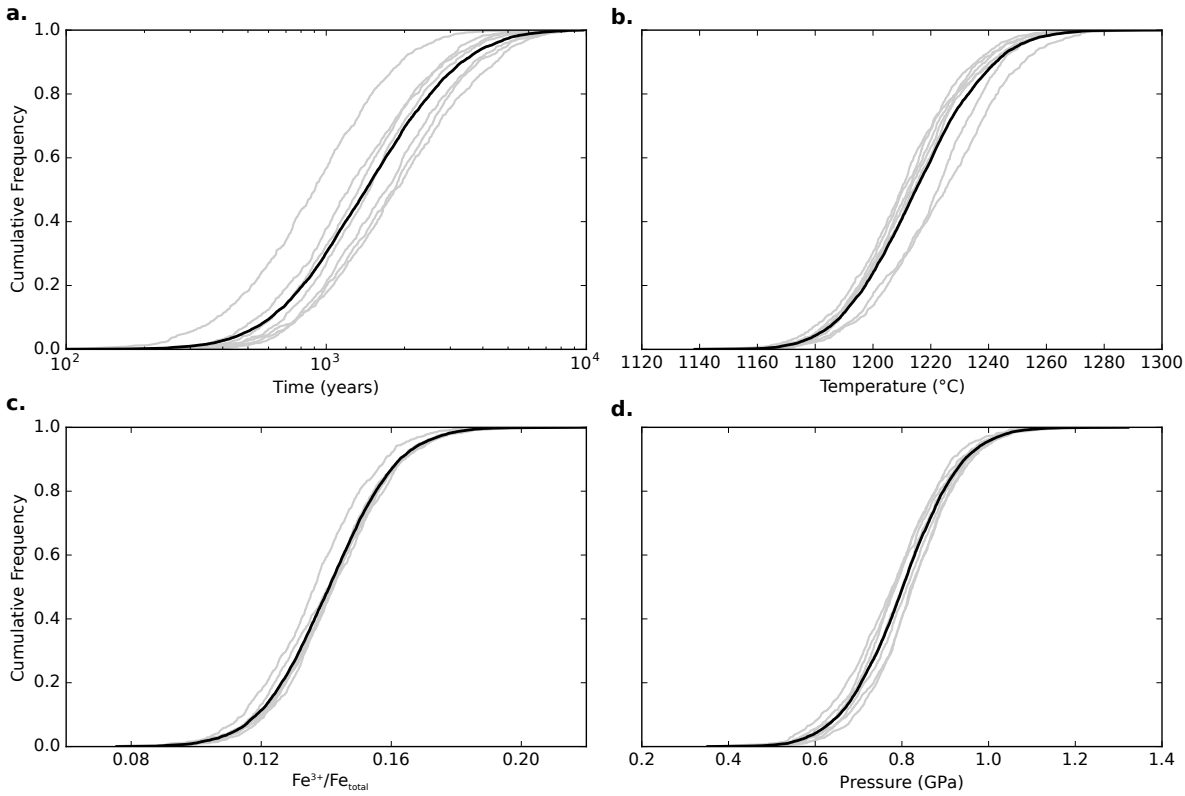

Fig. S9: Cumulative frequency distributions for parameters estimated from the Bayesian inversion for Cr-Al interdiffusion in Cr-spinels. **a**, time (years); **b**, temperature (°C), **c**, Fe^{3+}/Fe_{total}; **d**, pressure (GPa).

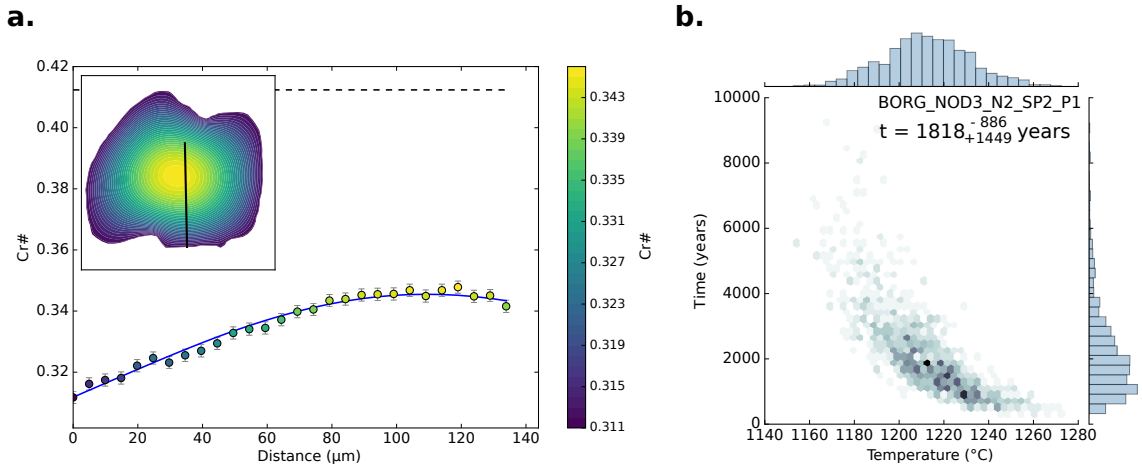

Fig. S10: Left: 1D Cr# profiles measured by electron microprobe (EPMA) across Borgarhraun spinels. Blue curves show the modelled 1D fit with maximised marginal likelihood parameters from the Bayesian inversion. The black lines show the constant initial condition used in the modelling, which was set at a Cr# of 0.412. Inset shows the maximum marginal likelihood solution for the 2D finite-element diffusion model of the spinels, which have been colour-coded based on Cr#; the black line marks the position of the EPMA profile. Right: Temperature-time density plots showing the trade-off between these posterior distributions from the Bayesian inversion for the model fits on the left. The exponential trade-offs between temperature and time are a culmination of the Arrhenius relationship between diffusivity and temperature. The individual posteriors are also shown as blue histograms on the axes. **a**, **b** correspond to profile BORG_NOD3_N2_SP2_P1.

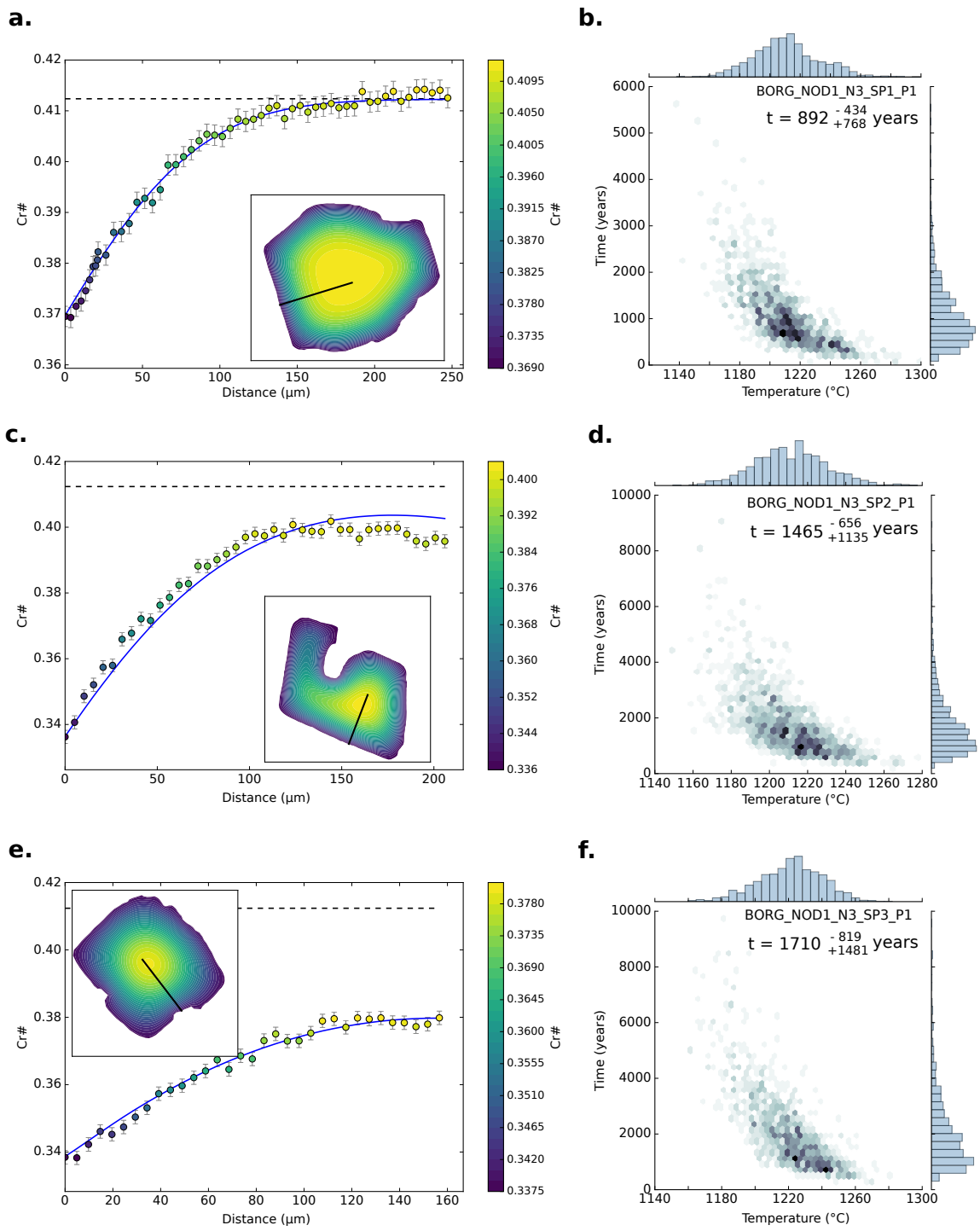

Fig. S11: See figure S10 for full caption. Profiles shown are: BORG_NOD1_N3_SP1_P1, **a**, **b**; BORG_NOD1_N3_SP2_P1, **c**, **d**; and BORG_NOD1_N3_SP3_P1, **e**, **f**.

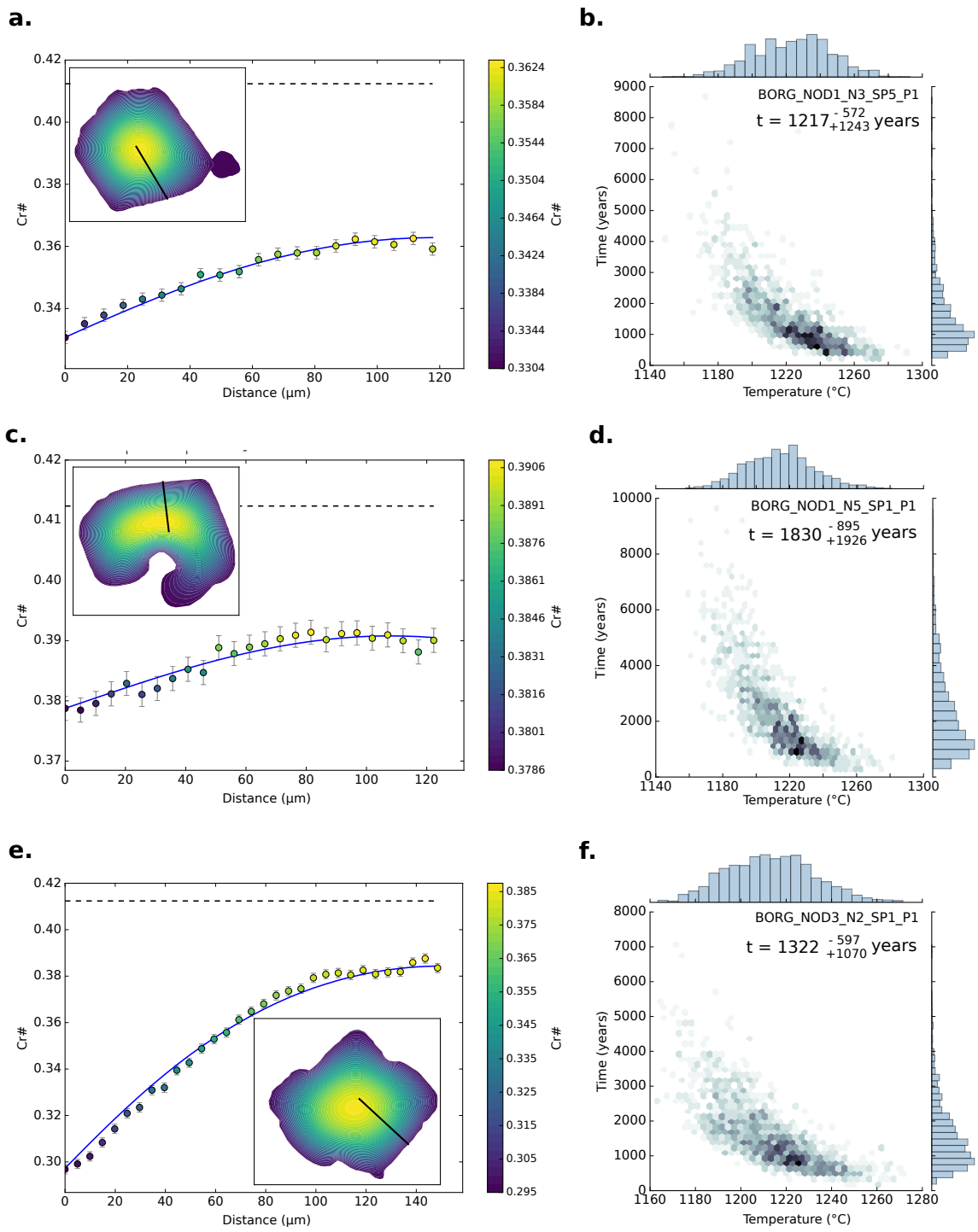

Fig. S12: See figure S10 for full caption. Profiles shown are: BORG_NOD1_N3_SP5_P1, **a**, **b**; BORG_NOD1_N5_SP1_P1, **c**, **d**; and BORG_NOD3_N2_SP1_P1, **e**, **f**.

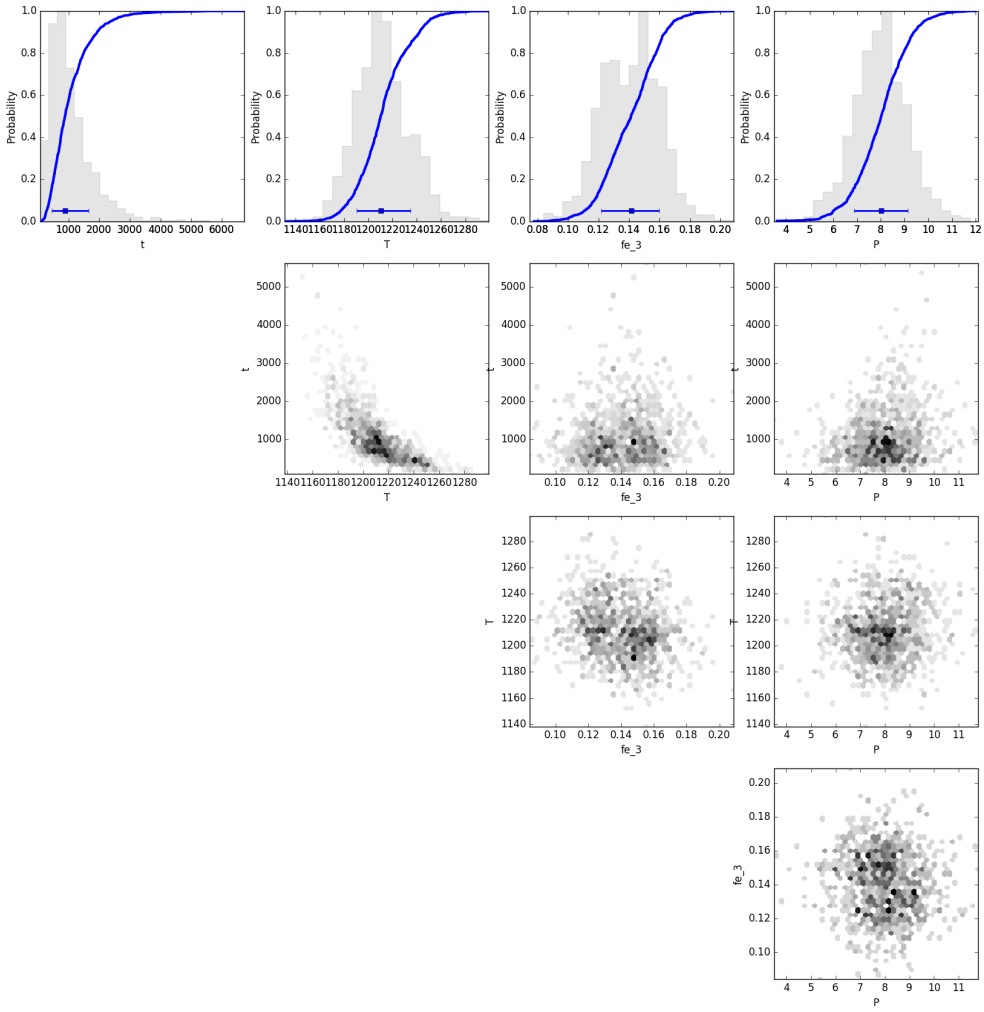

Fig. S13: Marginal plot showing the posterior distributions of the nested sampling Bayesian inversion for the main intensive parameters for spinel BORG_NOD1_N3_SP1_P1: t is time (days), T is temperature (°C), fe_3 is ferric iron content of the system and P is pressure (kbar). The top row shows histograms (grey bars) and probability density functions (blue curves) of the aforementioned intensive parameters. The blue bar shows the median result and 1σ standard deviation. The bottom three rows are density plots that show the trade-offs between the different intensive parameters.

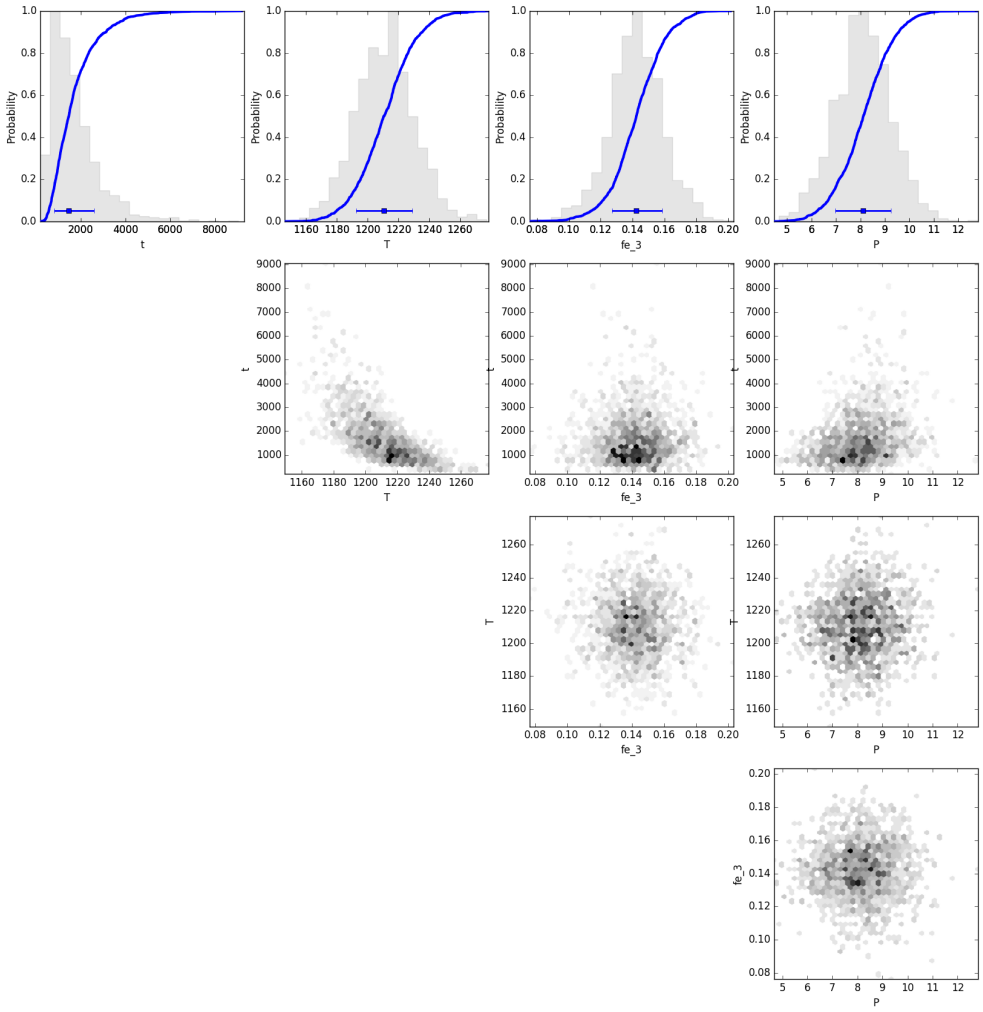

Fig. S14: Marginal plot showing the posterior distributions of the nested sampling Bayesian inversion for the main intensive parameters for spinel BORG_NOD1_N3_SP2_P1: t is time (days), T is temperature (°C), fe_3 is ferric iron content of the system and P is pressure (kbar). The top row shows histograms (grey bars) and probability density functions (blue curves) of the aforementioned intensive parameters. The blue bar shows the median result and 1σ standard deviation. The bottom three rows are density plots that show the trade-offs between the different intensive parameters.

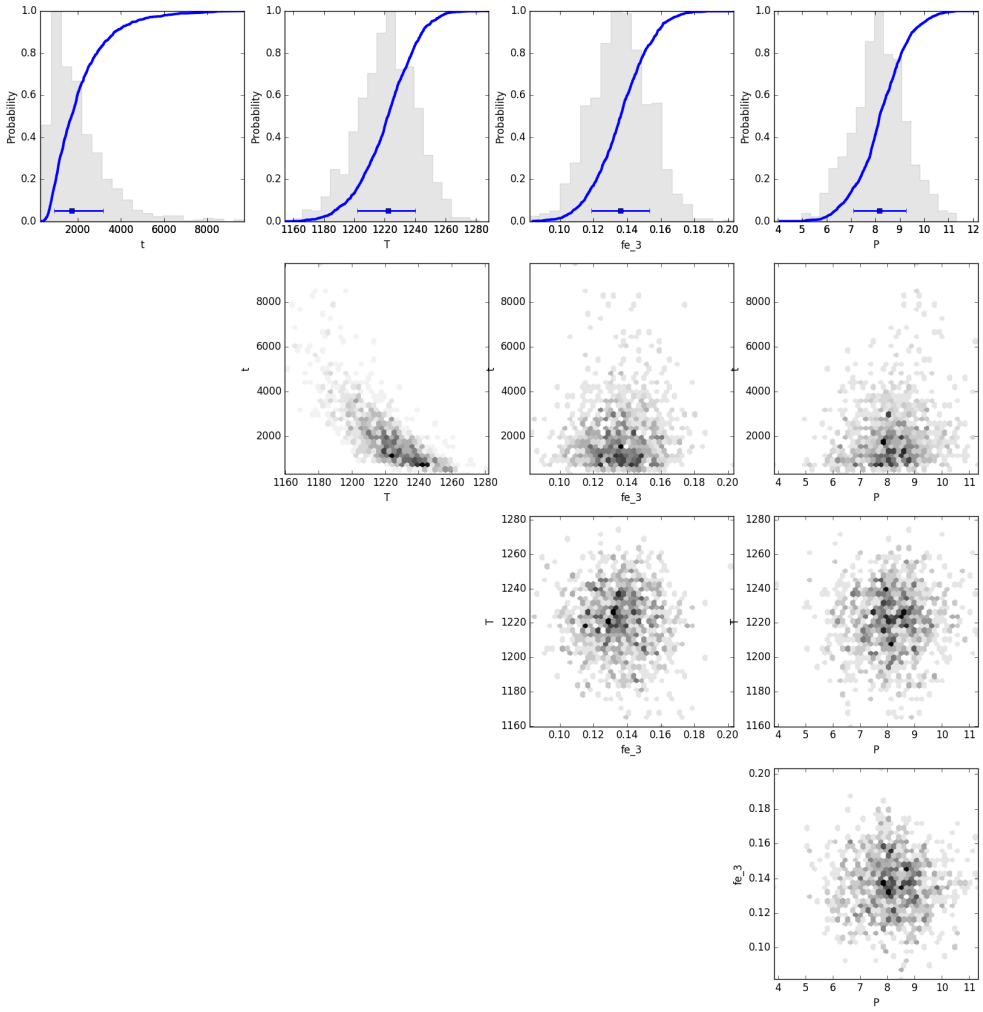

Fig. S15: Marginal plot showing the posterior distributions of the nested sampling Bayesian inversion for the main intensive parameters for spinel BORG_NOD1_N3_SP3_P1: t is time (days), T is temperature (°C), fe_3 is ferric iron content of the system and P is pressure (kbar). The top row shows histograms (grey bars) and probability density functions (blue curves) of the aforementioned intensive parameters. The blue bar shows the median result and 1σ standard deviation. The bottom three rows are density plots that show the trade-offs between the different intensive parameters.

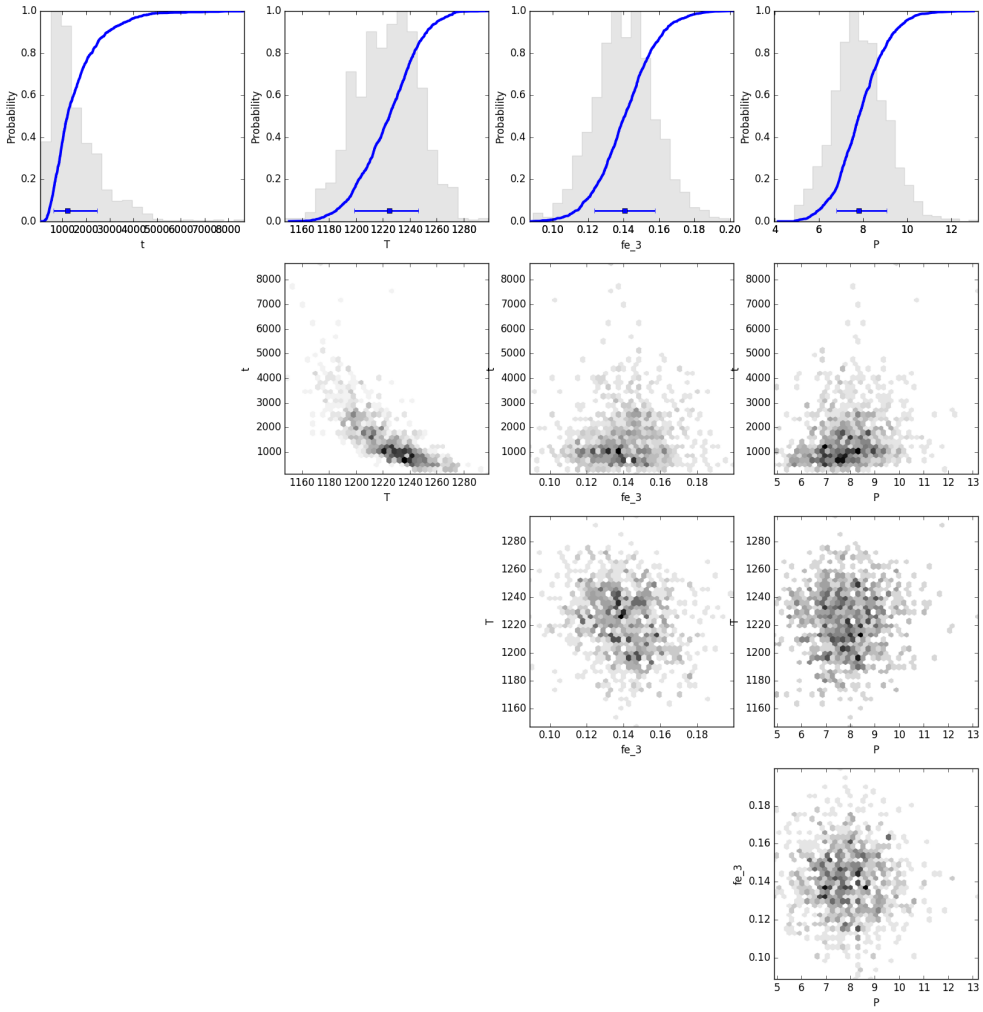

Fig. S16: Marginal plot showing the posterior distributions of the nested sampling Bayesian inversion for the main intensive parameters for spinel BORG_NOD1_N3_SP5_P1: t is time (days), T is temperature (°C), fe_3 is ferric iron content of the system and P is pressure (kbar). The top row shows histograms (grey bars) and probability density functions (blue curves) of the aforementioned intensive parameters. The blue bar shows the median result and 1σ standard deviation. The bottom three rows are density plots that show the trade-offs between the different intensive parameters.

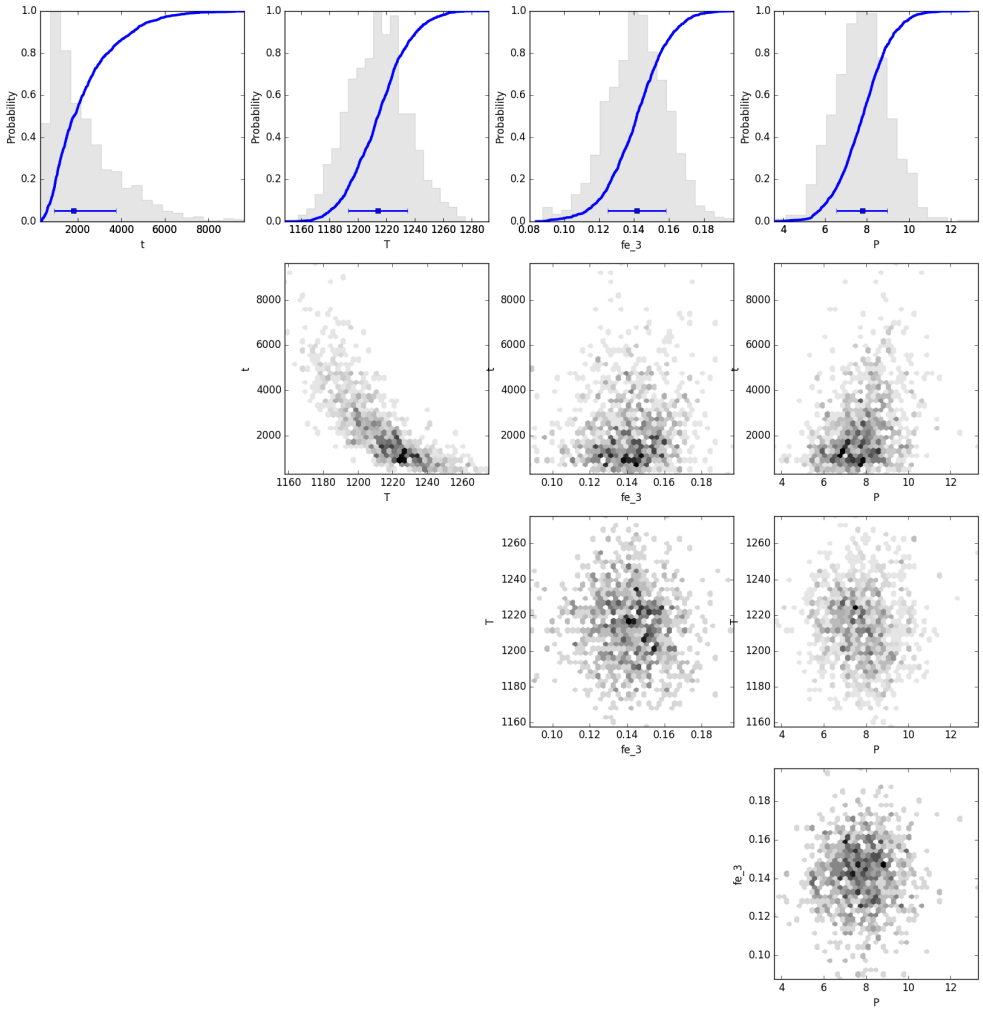

Fig. S17: Marginal plot showing the posterior distributions of the nested sampling Bayesian inversion for the main intensive parameters for spinel BORG_NOD1_N3_SP1_P1: t is time (days), T is temperature (°C), fe_3 is ferric iron content of the system and P is pressure (kbar). The top row shows histograms (grey bars) and probability density functions (blue curves) of the aforementioned intensive parameters. The blue bar shows the median result and 1σ standard deviation. The bottom three rows are density plots that show the trade-offs between the different intensive parameters.

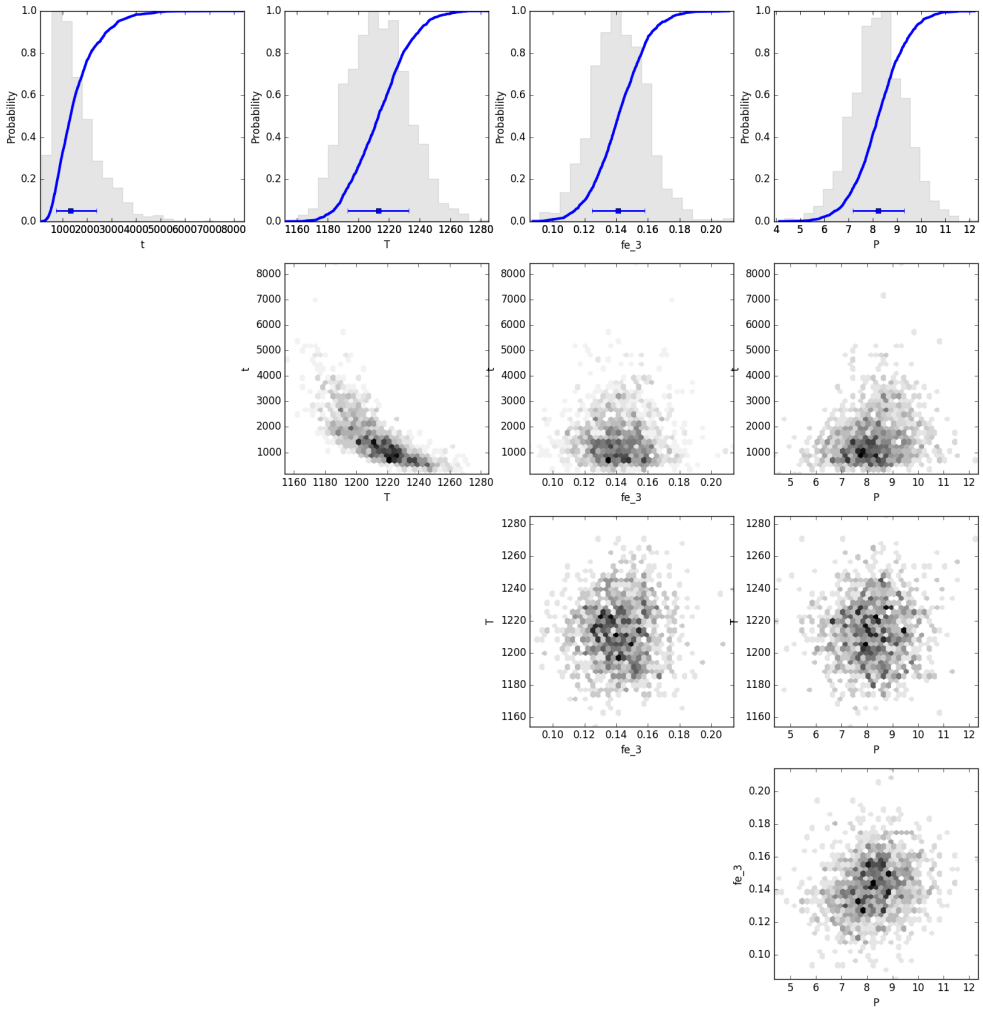

Fig. S18: Marginal plot showing the posterior distributions of the nested sampling Bayesian inversion for the main intensive parameters for spinel BORG_NOD1_N3_SP3_P1: t is time (days), T is temperature (°C), fe_3 is ferric iron content of the system and P is pressure (kbar). The top row shows histograms (grey bars) and probability density functions (blue curves) of the aforementioned intensive parameters. The blue bar shows the median result and 1σ standard deviation. The bottom three rows are density plots that show the trade-offs between the different intensive parameters.

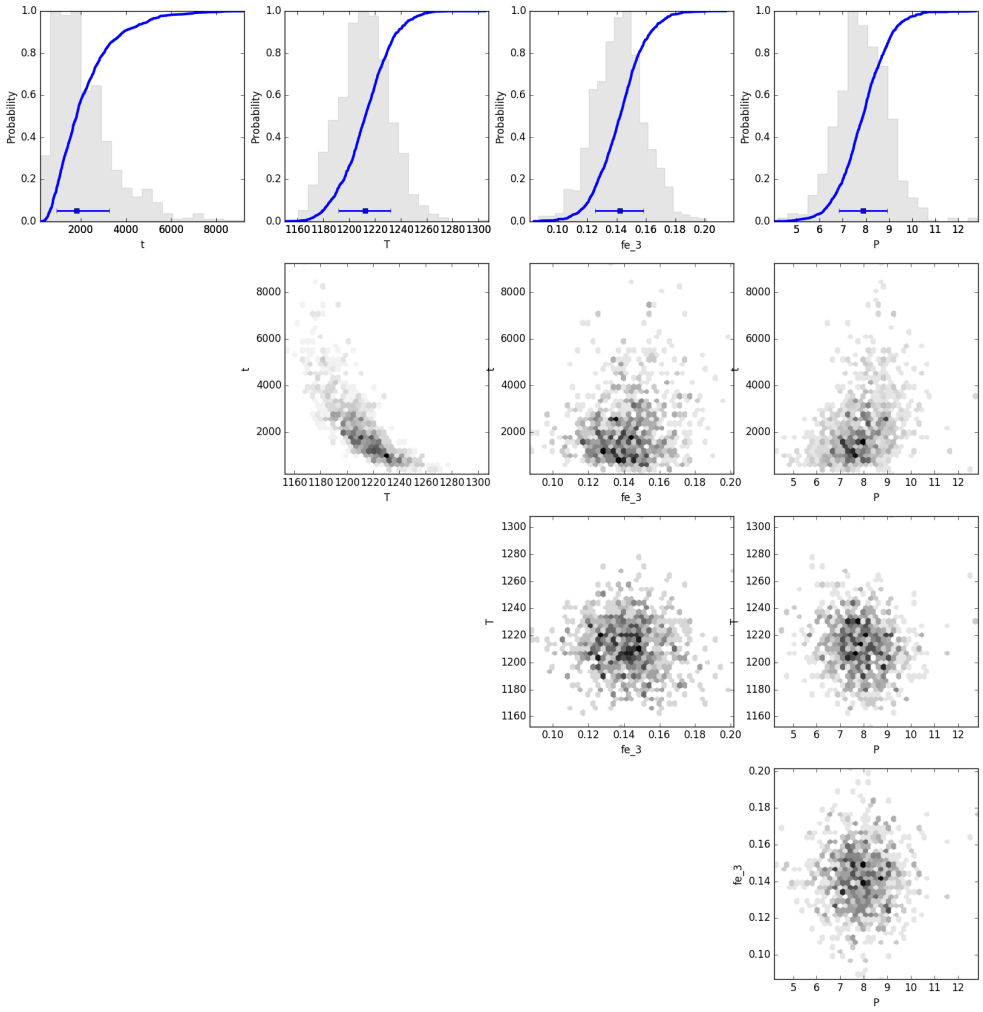

Fig. S19: Marginal plot showing the posterior distributions of the nested sampling Bayesian inversion for the main intensive parameters for spinel BORG_NOD1_N3_SP3_P2: t is time (days), T is temperature (°C), fe_3 is ferric iron content of the system and P is pressure (kbar). The top row shows histograms (grey bars) and probability density functions (blue curves) of the aforementioned intensive parameters. The blue bar shows the median result and 1σ standard deviation. The bottom three rows are density plots that show the trade-offs between the different intensive parameters.

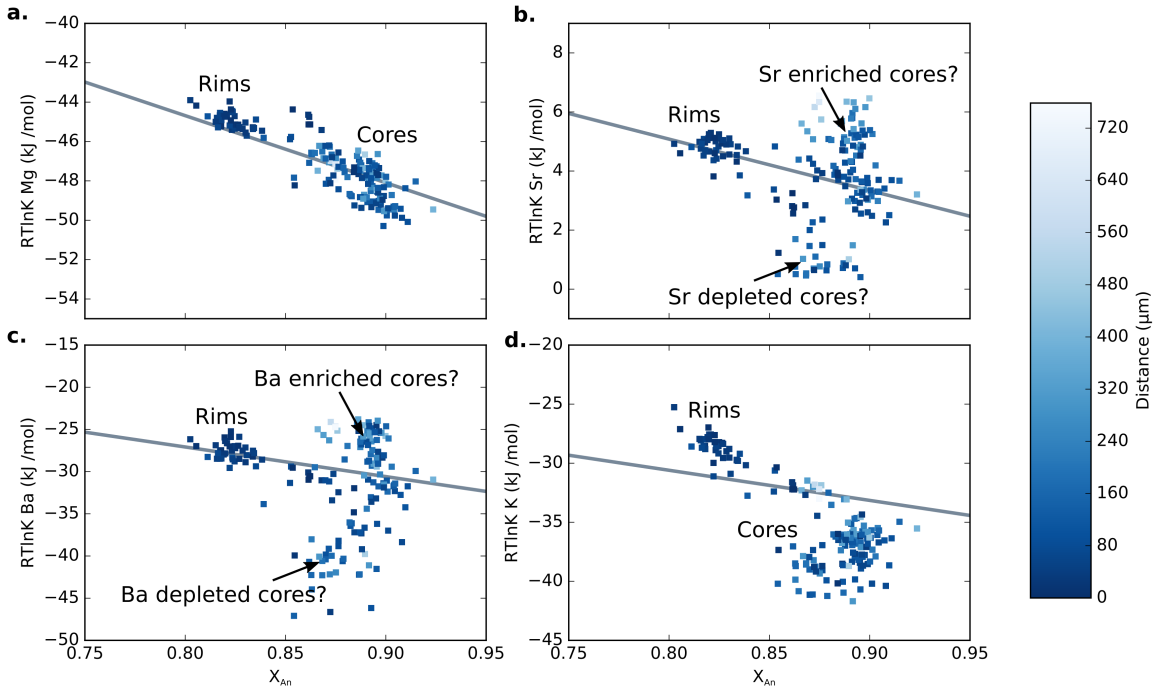

Fig. S20: Calculated partition coefficients (RTlnK) vs. anorthite content (X_{An}) for plagioclase trace-element profiles measured by SIMS (squares). Partition coefficients for Mg (**a**), Sr (**b**), Ba (**c**) and K (**d**) are shown and were calculated using the estimated temperature of the carrier liquid (1230 °C) (*63*). Mg, Sr, Ba and K partitioning coefficients were calculated with a melt composition with an MgO of 9.3 wt. %, Sr content of 97 ppm, Ba content of 25 ppm and K_2O content of 0.09 wt.%. Each point is colour-coded for the distance from the edge of the crystal. The grey lines are predictive partitioning models established for plagioclase: Mg uses the calibration of Bindeman et al. (*64*); Sr and Ba use Dohmen and Blundy (*65*), and K uses Bindeman et al. (*64*). The measured plagioclase crystals have calculated Mg partition coefficients that fall on a single array suggesting that there is likely some equilibrium in crystal cores for this element. Sr and Ba show a much wider spread in core compositions which could be due to crystallisation from variably enriched primary melts and that intercrystalline and intracrystalline disequilibrium exists.

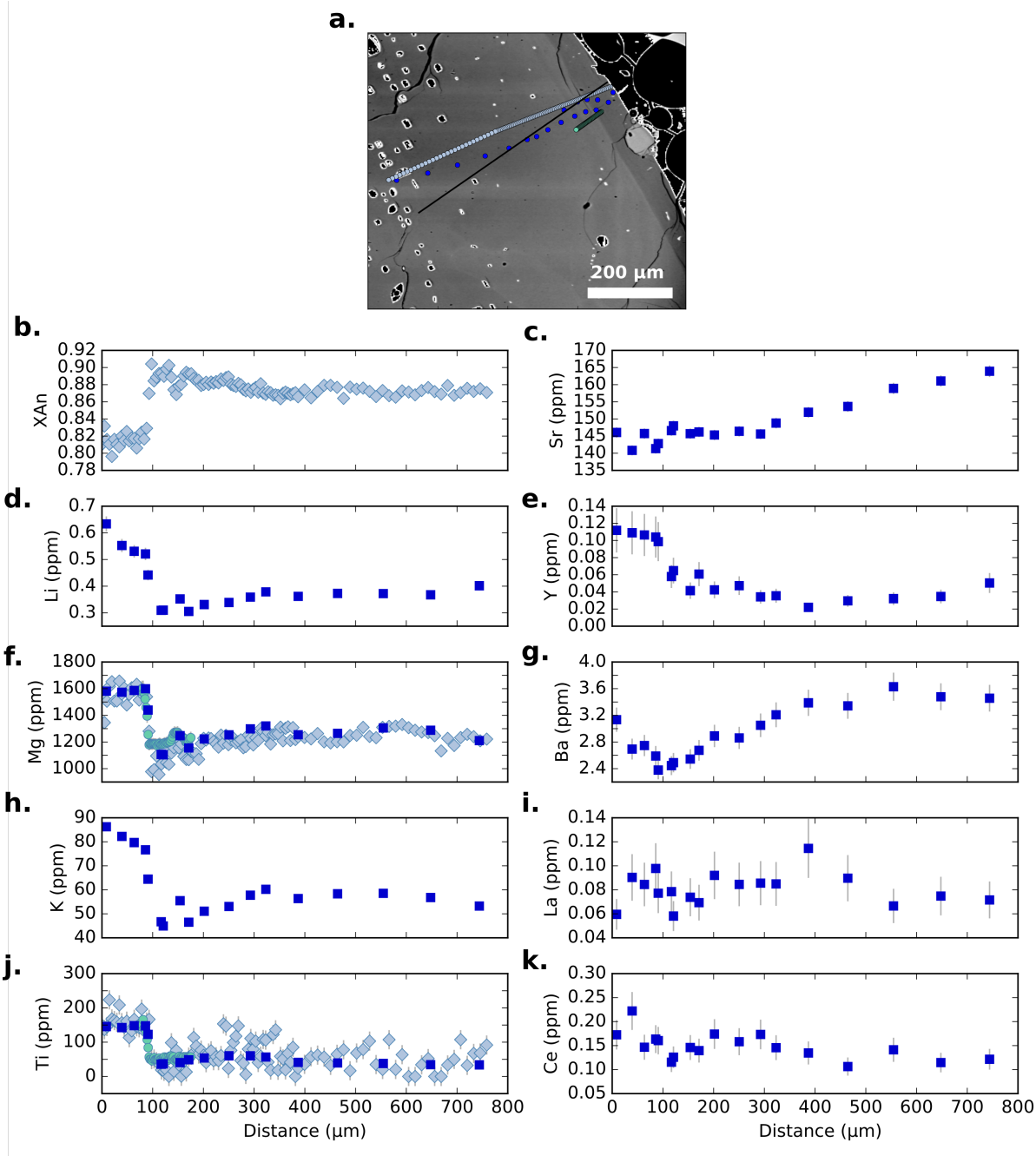

Fig. S21: Compositional profiles across Borgarhraun plagioclase crystal BORG_1_C1_P2, which shows evidence of core equilibrium for Mg, but possible disequilibrium for the other trace elements. **a** is a BSE image of the crystal showing the location of the measured profiles. Dark blue points are SIMS coarse spots, light blue points are EPMA spots, and turquoise points are SIMS step scan spots. These colours are also the same in the profile plots (**b**-**k**). The black line in **a** is where all of the compositional data are projected. Elements plotted include: anorthite content in mole fraction (**b**), Sr (**c**), Li (**d**), Y(**e**), Mg (**f**), Ba (**g**), K (**h**), La (**i**), Ti (**l**), and Ce (**k**). Profiles are defined by a near homogeneous core surrounded by a sharp rim.

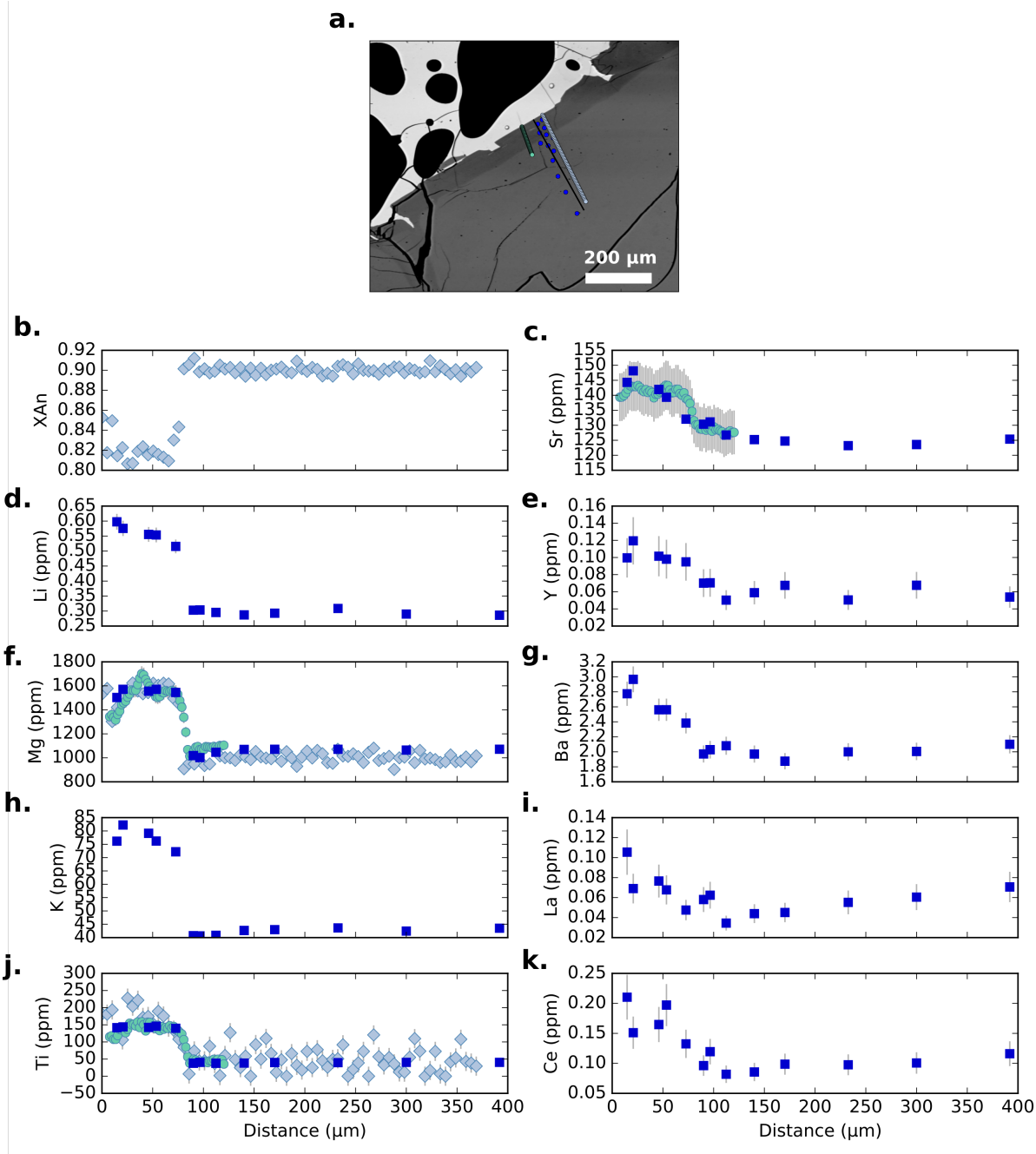

Fig. S22: Compositional profiles across Borgarhraun plagioclase crystal BORG_1_C3_P1. **a** is a BSE image of the crystal showing the location of the measured profiles. Dark blue points are SIMS coarse spots, light blue points are EPMA spots, and turquoise points are SIMS step scan spots. These colours are also the same in the profile plots (**b**-**k**). The black line in **a** is where all of the compositional data are projected. Elements plotted include: anorthite content in mole fraction (**b**), Sr (**c**), Li (**d**), Y(**e**), Mg (**f**), Ba (**g**), K (**h**), La (**i**), Ti (**l**), and Ce (**k**).

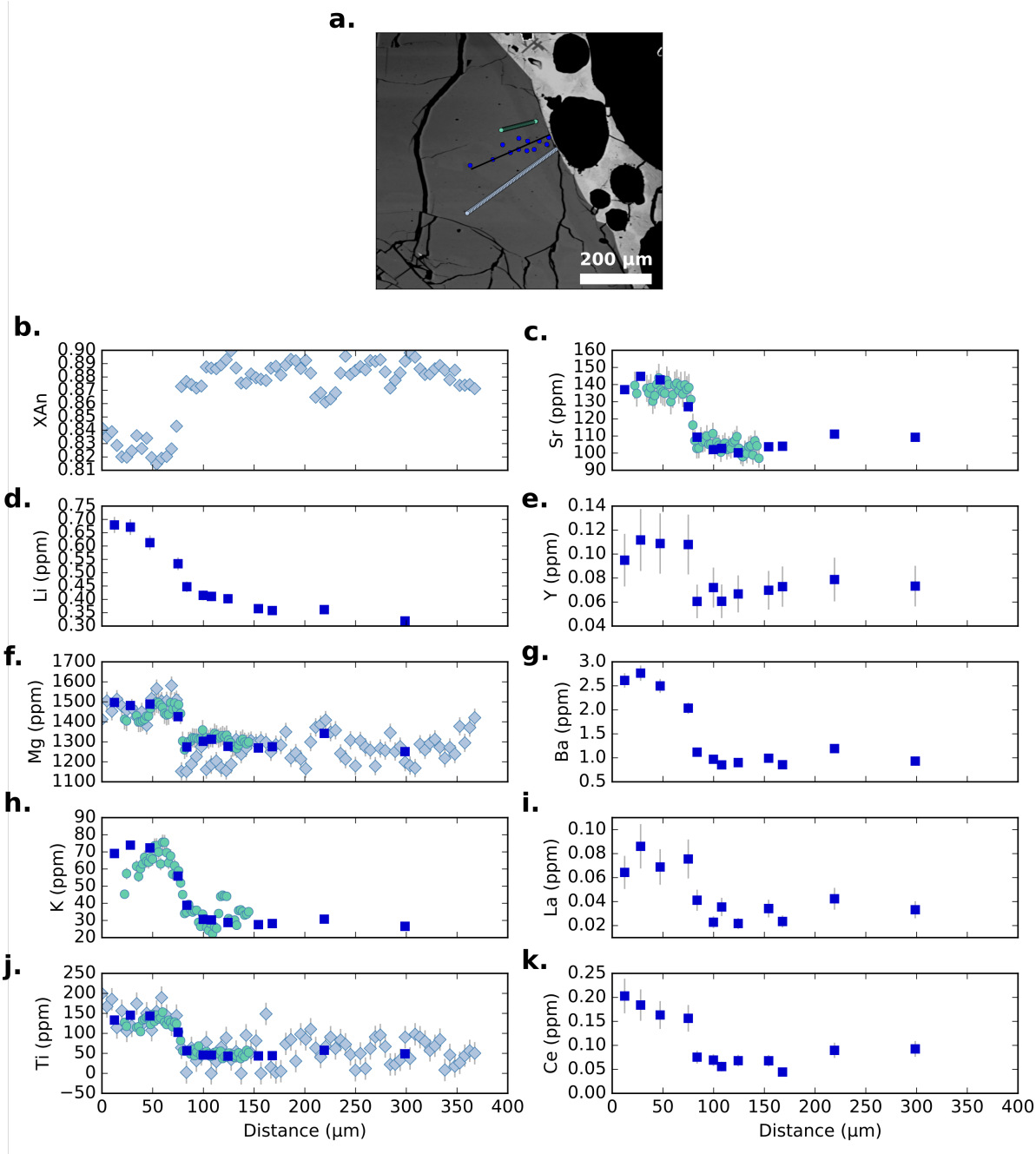

Fig. S23: Compositional profiles across Borgarhraun plagioclase crystal BORG_1_C5_P1. **a** is a BSE image of the crystal showing the location of the measured profiles. Dark blue points are SIMS coarse spots, light blue points are EPMA spots, and turquoise points are SIMS step scan spots. These colours are also the same in the profile plots (**b**-**k**). The black line in **a** is where all of the compositional data are projected. Elements plotted include: anorthite content in mole fraction (**b**), Sr (**c**), Li (**d**), Y(**e**), Mg (**f**), Ba (**g**), K (**h**), La (**i**), Ti (**l**), and Ce (**k**).

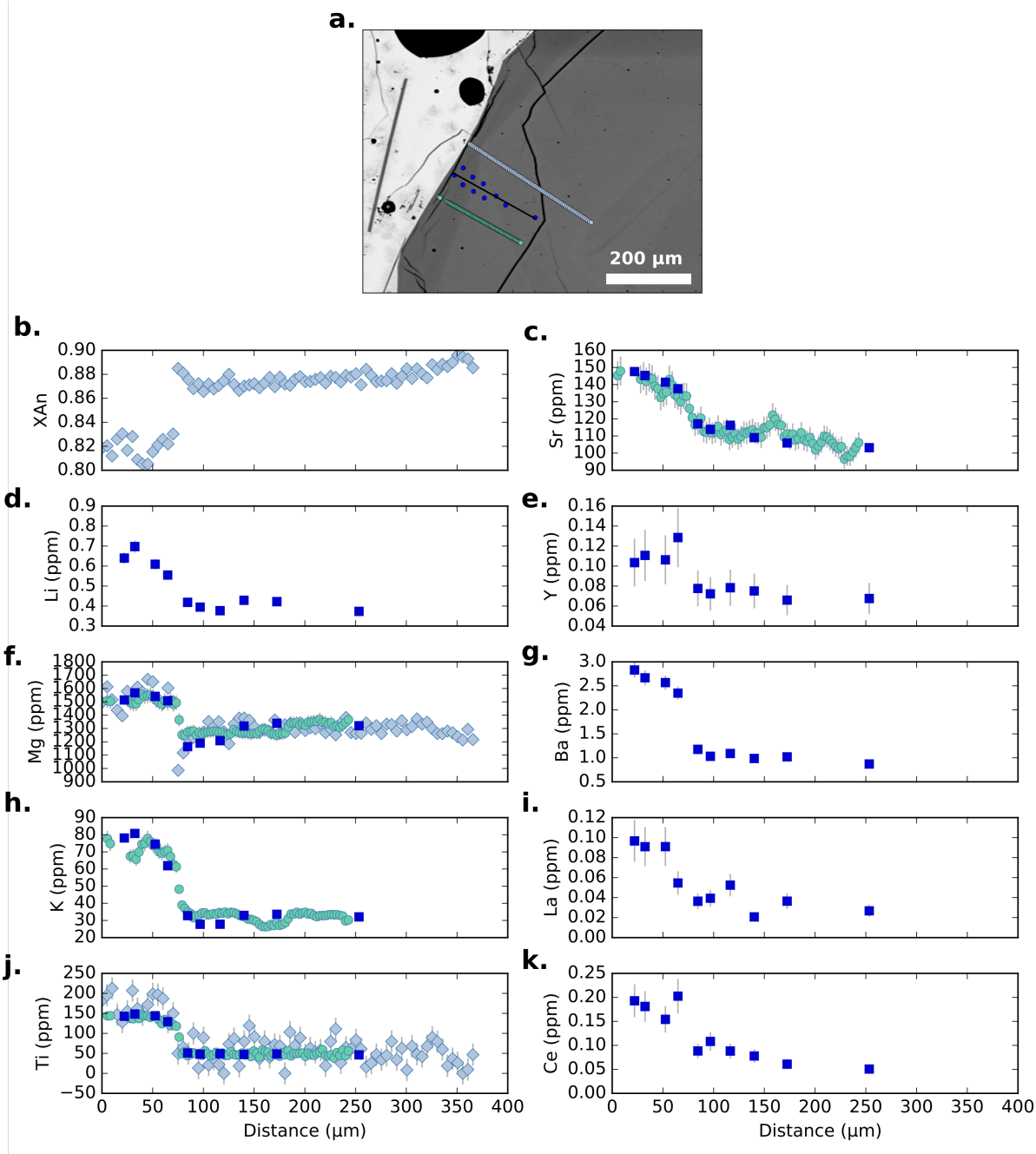

Fig. S24: Compositional profiles across Borgarhraun plagioclase crystal BORG_1_C6_P1. **a** is a BSE image of the crystal showing the location of the measured profiles. Dark blue points are SIMS coarse spots, light blue points are EPMA spots, and turquoise points are SIMS step scan spots. These colours are also the same in the profile plots (**b**-**k**). The black line in **a** is where all of the compositional data are projected. Elements plotted include: anorthite content in mole fraction (**b**), Sr (**c**), Li (**d**), Y(**e**), Mg (**f**), Ba (**g**), K (**h**), La (**i**), Ti (**l**), and Ce (**k**).

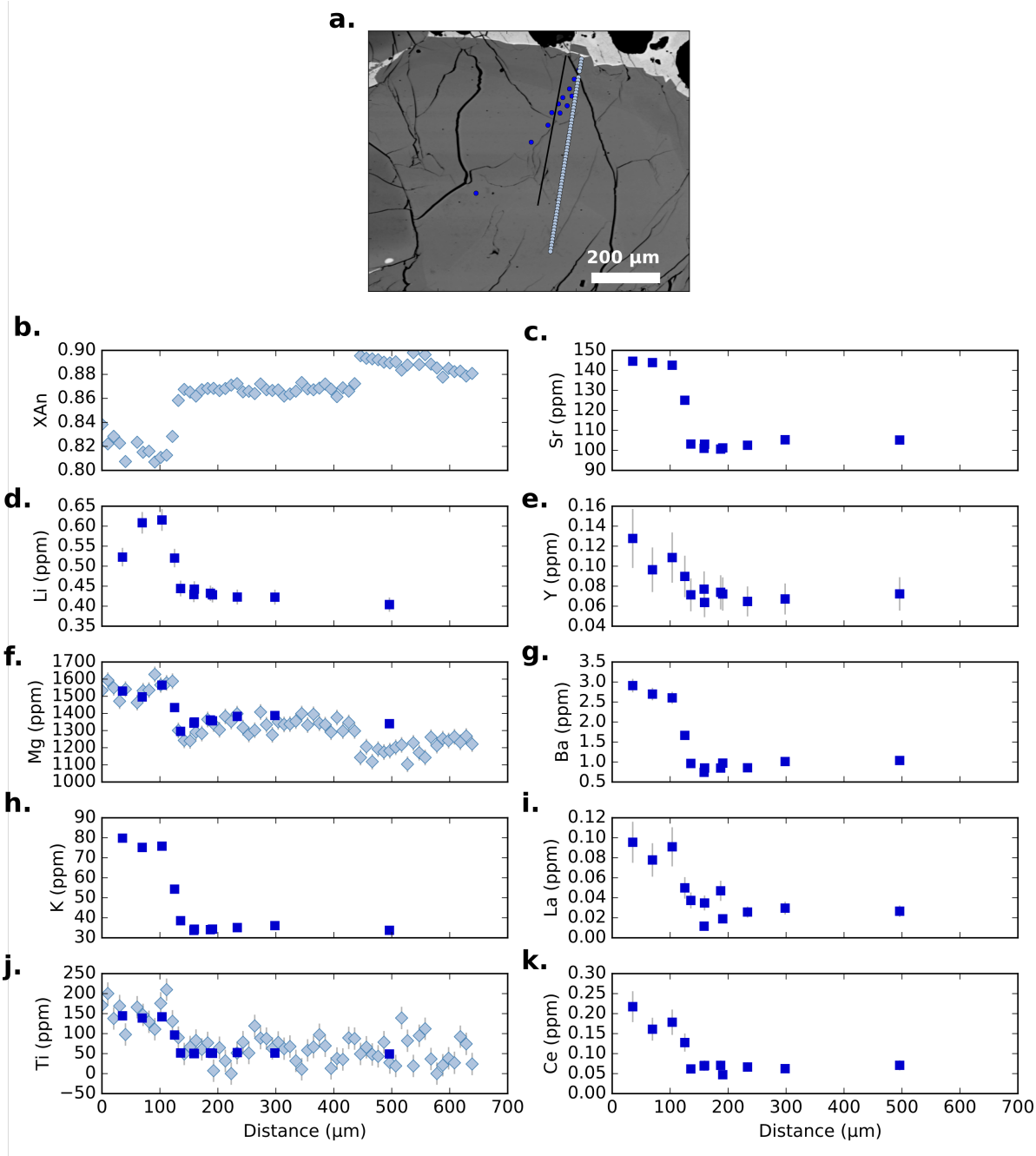

Fig. S25: Compositional profiles across Borgarhraun plagioclase crystal BORG_1_C7_P1. **a** is a BSE image of the crystal showing the location of the measured profiles. Dark blue points are SIMS coarse spots, light blue points are EPMA spots, and turquoise points are SIMS step scan spots. These colours are also the same in the profile plots (**b**-**k**). The black line in **a** is where all of the compositional data are projected. Elements plotted include: anorthite content in mole fraction (**b**), Sr (**c**), Li (**d**), Y(**e**), Mg (**f**), Ba (**g**), K (**h**), La (**i**), Ti (**l**), and Ce (**k**).

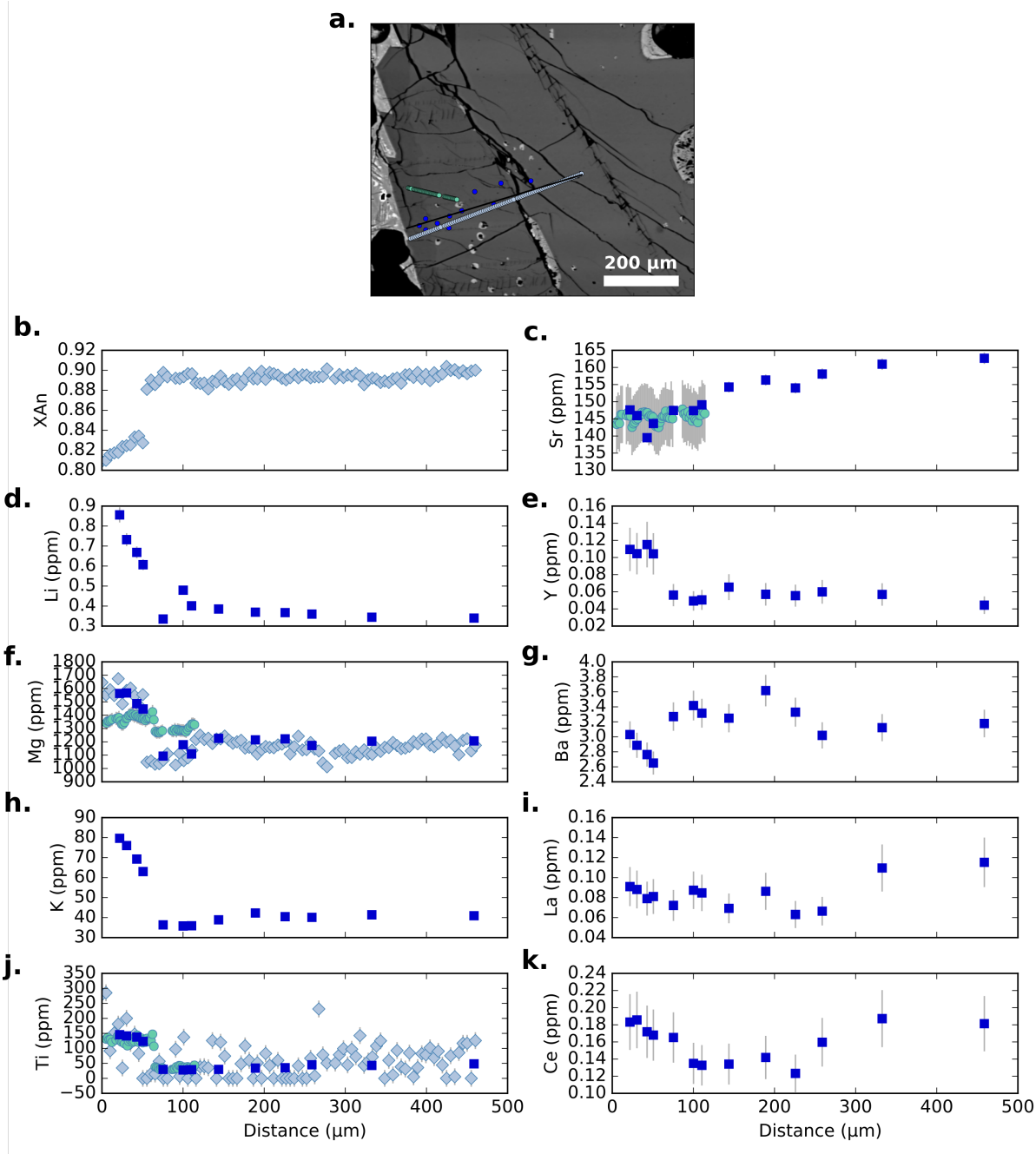

Fig. S26: Compositional profiles across Borgarhraun plagioclase crystal BORG_2_C1_P1. **a** is a BSE image of the crystal showing the location of the measured profiles. Dark blue points are SIMS coarse spots, light blue points are EPMA spots, and turquoise points are SIMS step scan spots. These colours are also the same in the profile plots (**b**-**k**). The black line in **a** is where all of the compositional data are projected. Elements plotted include: anorthite content in mole fraction (**b**), Sr (**c**), Li (**d**), Y(**e**), Mg (**f**), Ba (**g**), K (**h**), La (**i**), Ti (**l**), and Ce (**k**).

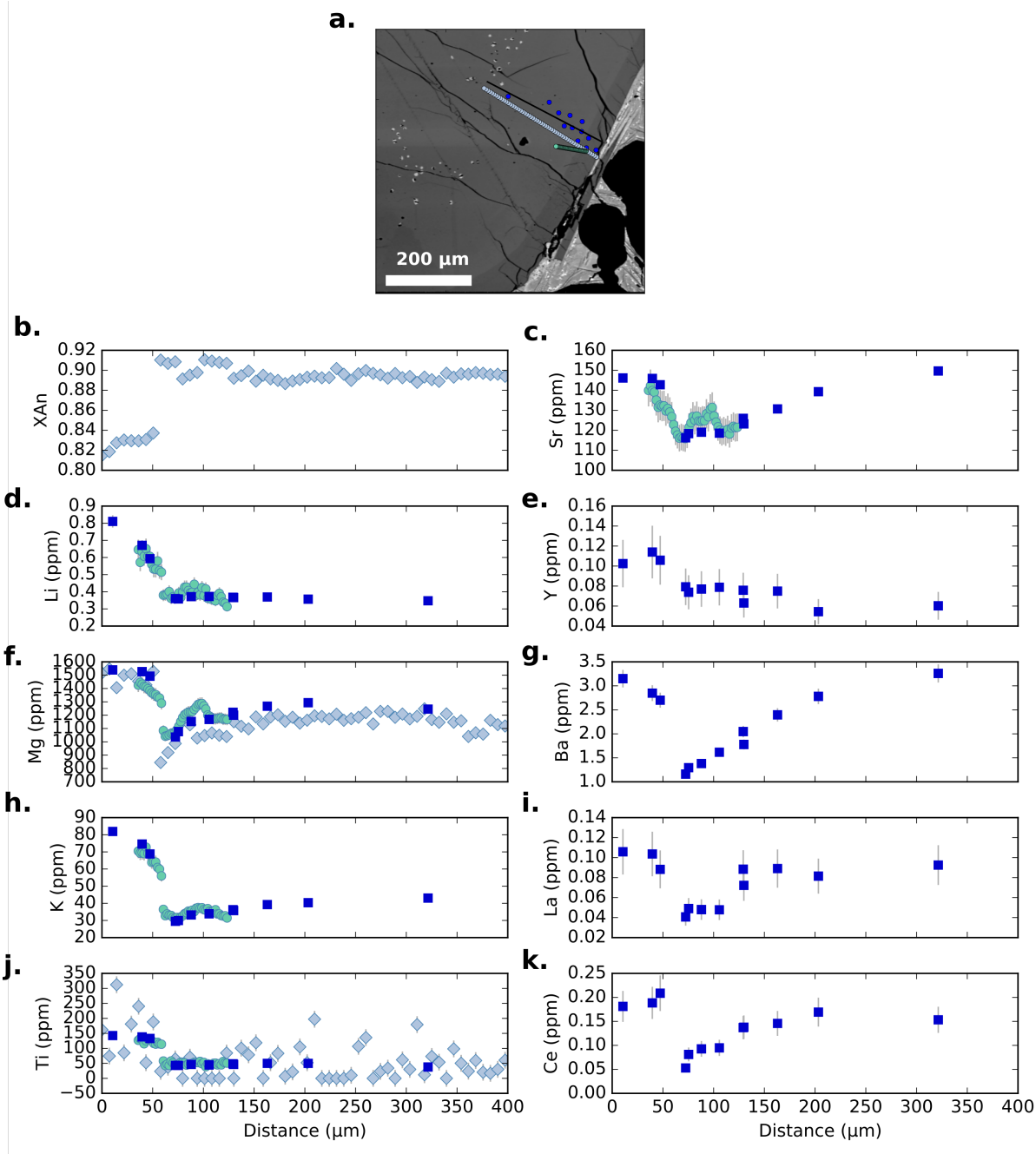

Fig. S27: Compositional profiles across Borgarhraun plagioclase crystal BORG_2_C1_P2. **a** is a BSE image of the crystal showing the location of the measured profiles. Dark blue points are SIMS coarse spots, light blue points are EPMA spots, and turquoise points are SIMS step scan spots. These colours are also the same in the profile plots (**b**-**k**). The black line in **a** is where all of the compositional data are projected. Elements plotted include: anorthite content in mole fraction (**b**), Sr (**c**), Li (**d**), Y(**e**), Mg (**f**), Ba (**g**), K (**h**), La (**i**), Ti (**l**), and Ce (**k**).

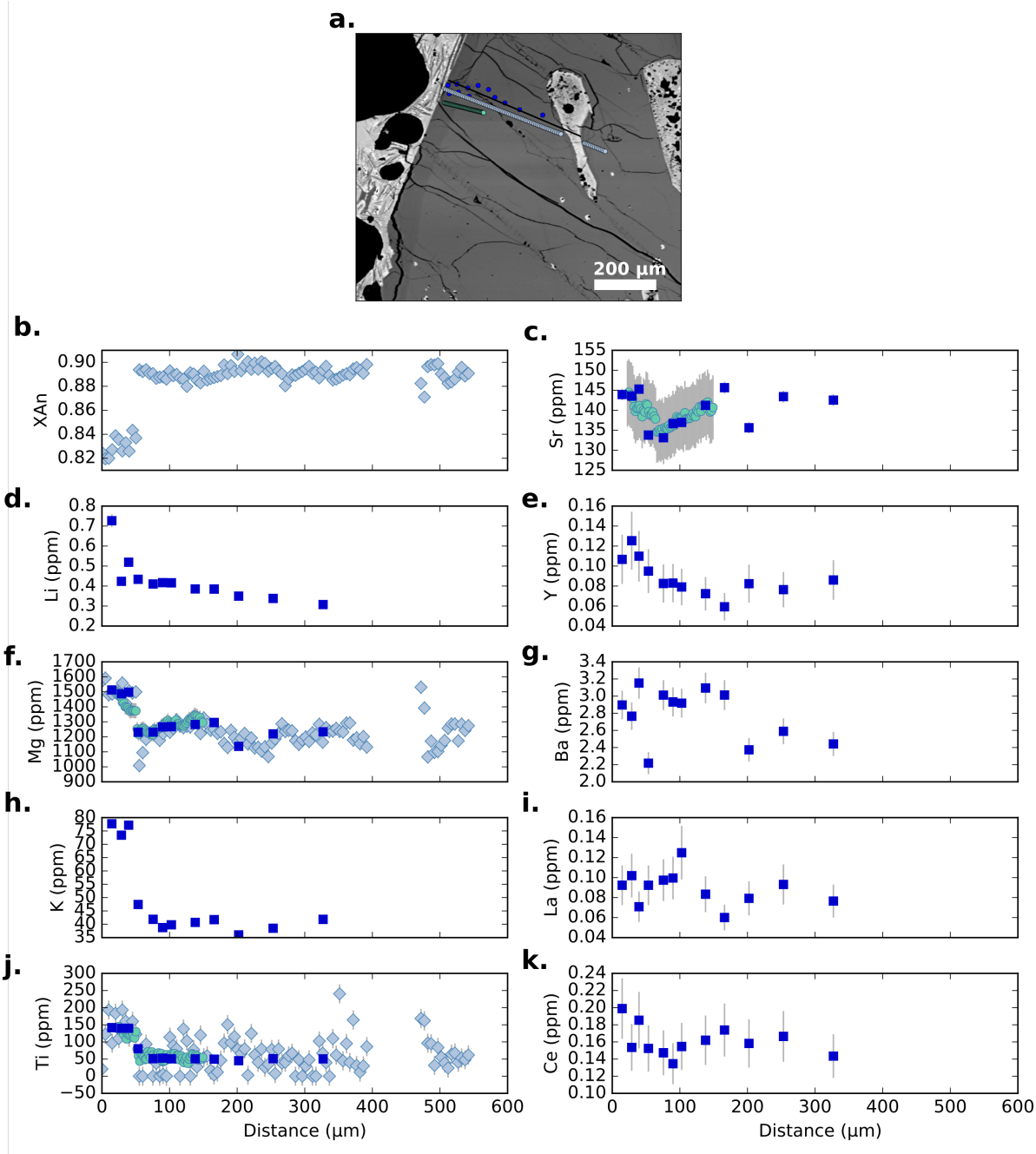

Fig. S28: Compositional profiles across Borgarhraun plagioclase crystal BORG_2_C2_P1. **a** is a BSE image of the crystal showing the location of the measured profiles. Dark blue points are SIMS coarse spots, light blue points are EPMA spots, and turquoise points are SIMS step scan spots. These colours are also the same in the profile plots (**b**-**k**). The black line in **a** is where all of the compositional data are projected. Elements plotted include: anorthite content in mole fraction (**b**), Sr (**c**), Li (**d**), Y(**e**), Mg (**f**), Ba (**g**), K (**h**), La (**i**), Ti (**l**), and Ce (**k**).

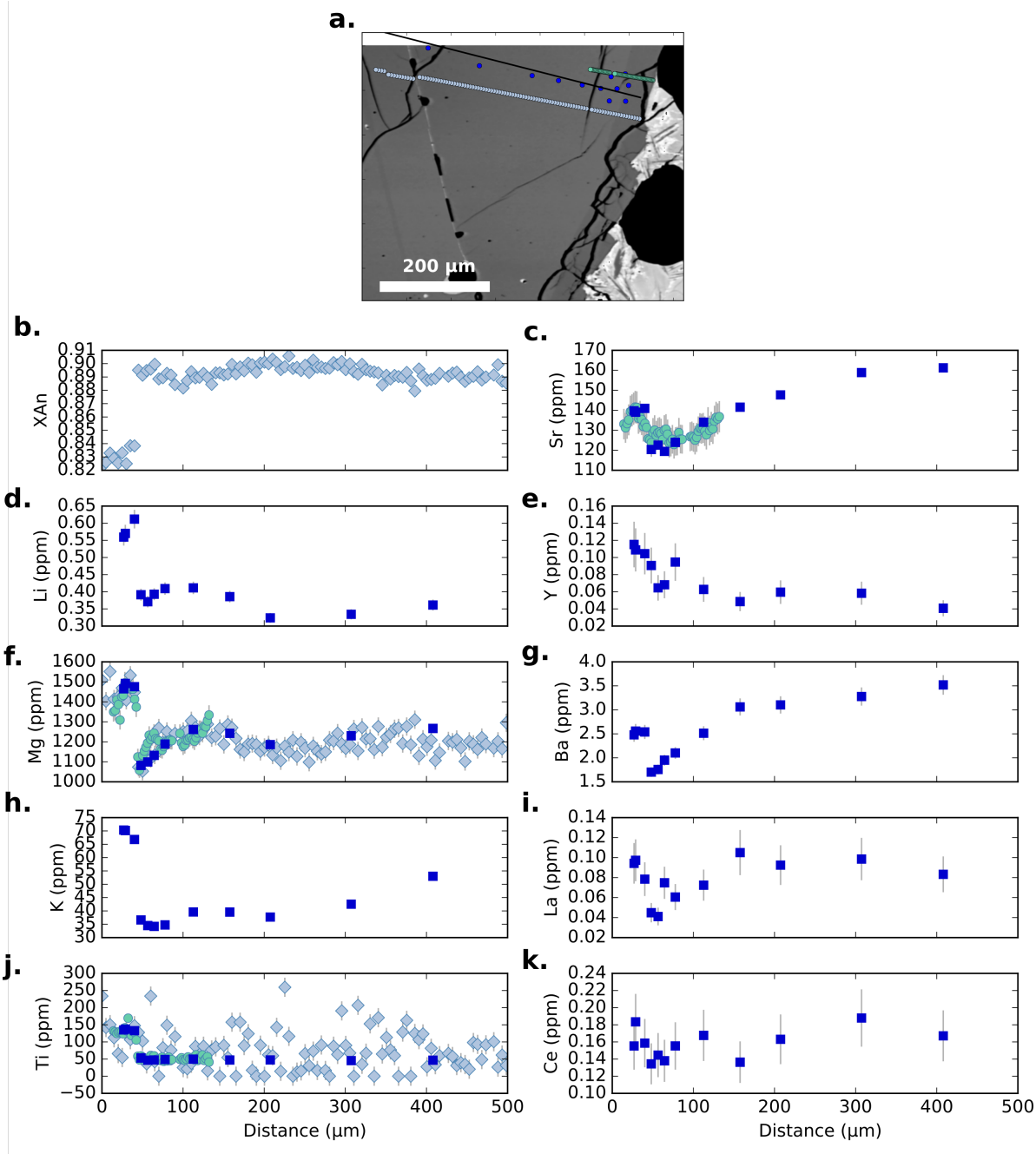

Fig. S29: Compositional profiles across Borgarhraun plagioclase crystal BORG_2_C2_P2. **a** is a BSE image of the crystal showing the location of the measured profiles. Dark blue points are SIMS coarse spots, light blue points are EPMA spots, and turquoise points are SIMS step scan spots. These colours are also the same in the profile plots (**b**-**k**). The black line in **a** is where all of the compositional data are projected. Elements plotted include: anorthite content in mole fraction (**b**), Sr (**c**), Li (**d**), Y(**e**), Mg (**f**), Ba (**g**), K (**h**), La (**i**), Ti (**l**), and Ce (**k**).

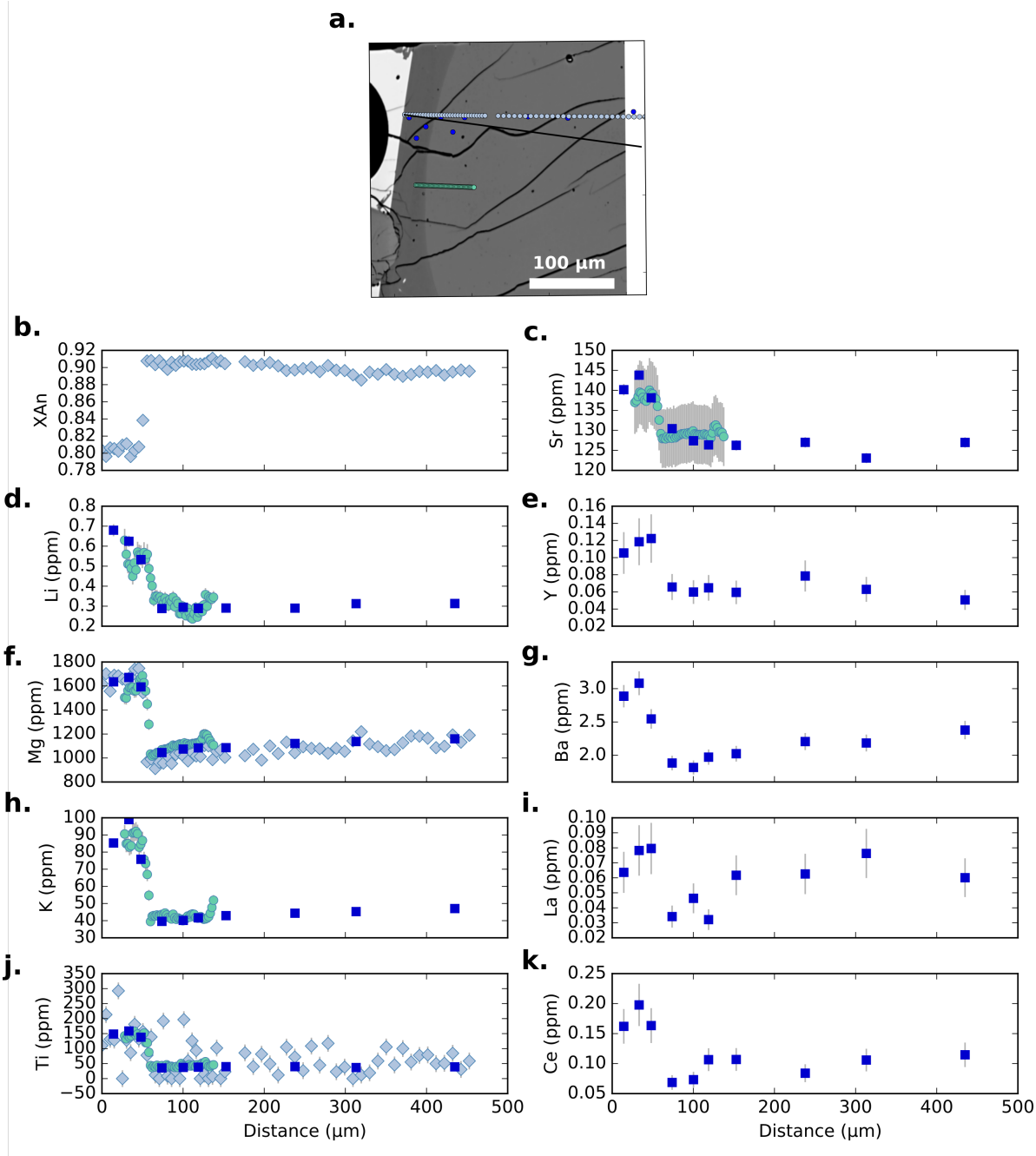

Fig. S30: Compositional profiles across Borgarhraun plagioclase crystal BORG_3_C7_P1. **a** is a BSE image of the crystal showing the location of the measured profiles. Dark blue points are SIMS coarse spots, light blue points are EPMA spots, and turquoise points are SIMS step scan spots. These colours are also the same in the profile plots (**b**-**k**). The black line in **a** is where all of the compositional data are projected. Elements plotted include: anorthite content in mole fraction (**b**), Sr (**c**), Li (**d**), Y(**e**), Mg (**f**), Ba (**g**), K (**h**), La (**i**), Ti (**l**), and Ce (**k**).

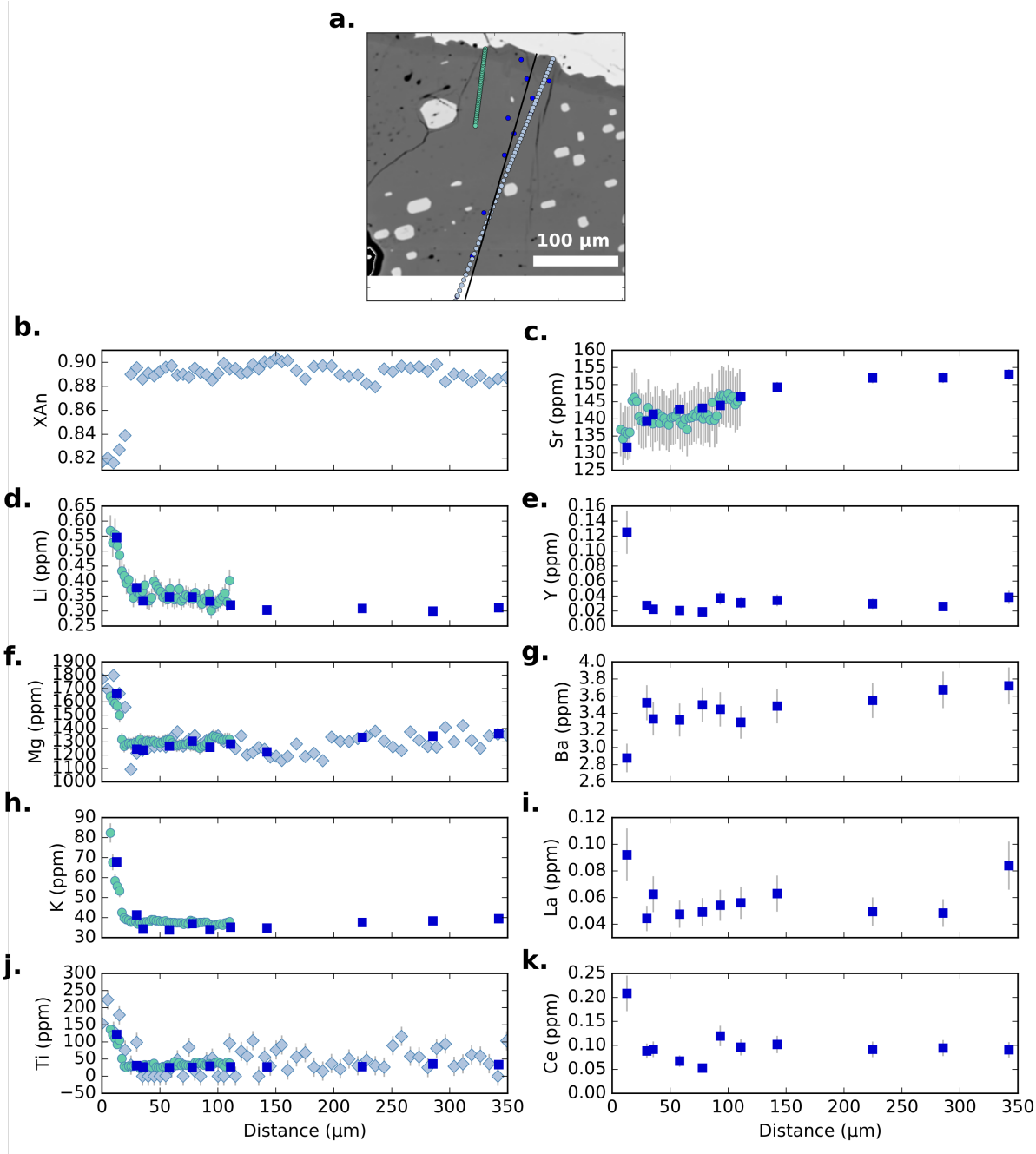

Fig. S31: Compositional profiles across Borgarhraun plagioclase crystal BORG_3_C10_P1. **a** is a BSE image of the crystal showing the location of the measured profiles. Dark blue points are SIMS coarse spots, light blue points are EPMA spots, and turquoise points are SIMS step scan spots. These colours are also the same in the profile plots (**b**-**k**). The black line in **a** is where all of the compositional data are projected. Elements plotted include: anorthite content in mole fraction (**b**), Sr (**c**), Li (**d**), Y(**e**), Mg (**f**), Ba (**g**), K (**h**), La (**i**), Ti (**l**), and Ce (**k**).

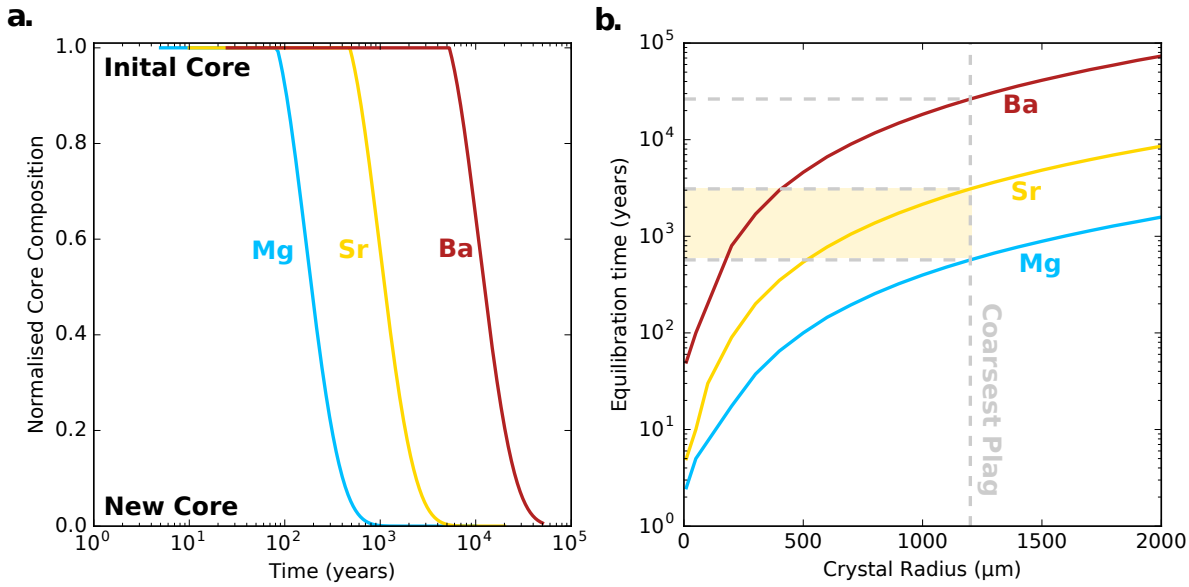

Fig. S32: Results of 3D spherical bulk diffusion in high-anorthite plagioclase cores. **a** shows how the central trace element composition of a spherical plagioclase core with a $1200\,\mu m$ radius changes with time. Mg is shown in blue, Sr in yellow and Ba in red. The core compositions have been normalised relative to the initial core composition and the new equilibrated compositions (see methods section for more detail), such that the former is equivalent to 1 and the latter is equivalent to 0. Slower diffusing elements such as Ba maintain their original core composition for much longer and thus take a longer time to equilibrate. **b** shows how crystal radius can affect the time in which the centre of the sphere acquires the new equilibrium concentration within analytical uncertainty (i.e. equilibration time). The coarsest observed crystal radius ($1200\,\mu m$) is marked on as a grey dashed line. The yellow region marks the area where the Borgarhraun plagioclase crystal cargo sits, which corresponds to the coarse plagioclase macrocrysts that show intracrystalline equilibrium for Mg (lower limit of residence time) and disequilibrium for Sr (upper limit of residence time). This is consistent with the storage times estimated from zoning in the spinels. Modelling was done at $1215\,^{\circ}C$.

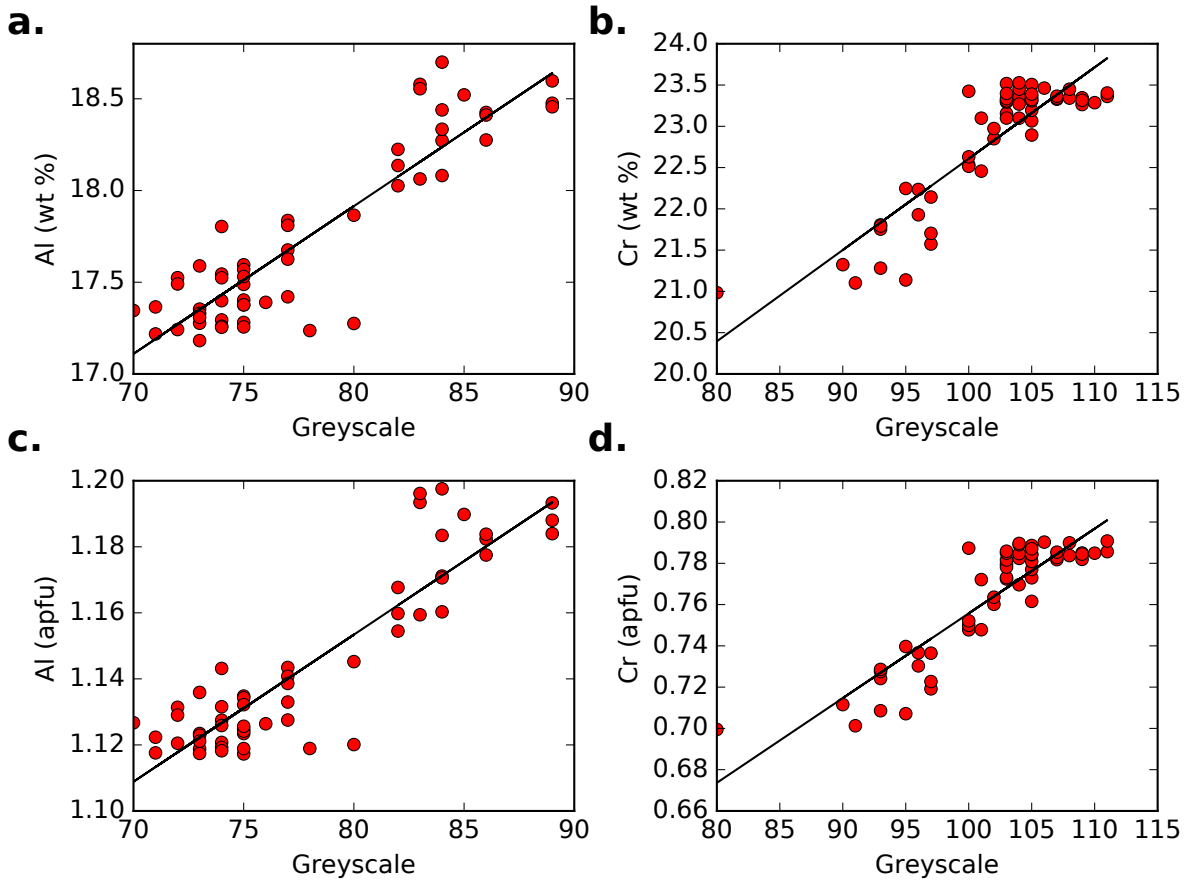

Fig. S33: Performance of the greyscale calibration when applied to spinels from BORG_NOD1_N3 (red points). Al (wt.%) vs. greyscale (**a**), Cr (wt.%) vs. greyscale (**b**), Al (apfu) vs. greyscale (**c**) and Cr (apfu) vs. greyscale (**d**) are shown. The black lines are the calibration curves.

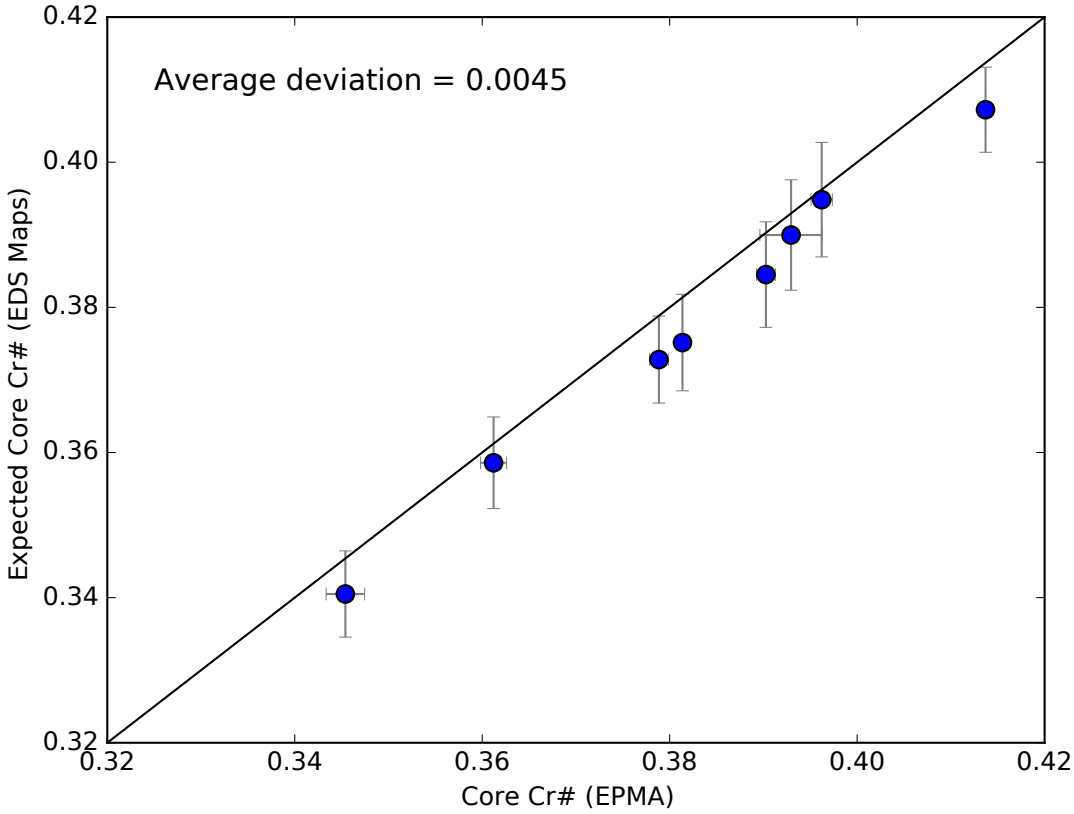

Fig. S34: Cr# predictions of spinel core compositions from the EDS map calibration compared to EPMA measurements. The black line is a 1:1 line. The error bars are 1σ standard deviations for mean analysis of each spinel core. The average deviation is shown in the top left corner.

Table S1: Diffusion coefficient regression parameters derived for Cr-Al interdiffusion in spinel using the data of Suzuki et al. (*24*) and Posner et al. (*25*).

Element	**a**	**b**	**h**	**q**	**j**	**v**
CrAl	-8.60E+00	9.16E-03	3.61E+00	-5.28E+04	6.03E-10	-9.59E-07

Table S2: Covariance matrix for Cr-Al interdiffusion in spinel derived in this study.

	a	**b**	**h**	**q**	**j**	**v**
a	1.47E+00	1.73E-03	-1.55E-01	-2.09E+03	-2.66E-10	3.86E-07
b	1.73E-03	3.33E-03	4.66E-04	1.13E+02	-1.97E-11	3.26E-08
h	-1.55E-01	4.66E-04	7.12E-02	2.29E+02	1.43E-11	-2.53E-08
q	-2.09E+03	1.13E+02	2.29E+02	7.02E+06	-2.71E-07	5.12E-04
j	-2.66E-10	-1.97E-11	1.43E-11	-2.71E-07	5.66E-19	-1.01E-15
v	3.86E-07	3.26E-08	-2.53E-08	5.12E-04	-1.01E-15	1.82E-12

Table S3: Median storage timescales and 1σ uncertainties from the Bayesian inversion of the spinel crystals modelled as part of this study.

Profile	**Median (years)**	**+ 1σ error (years)**	**- 1σ error (years)**
BORG_NOD1_N3_SP1_P1	892	768	434
BORG_NOD1_N3_SP2_P1	1465	1135	656
BORG_NOD1_N3_SP3_P1	1710	1481	819
BORG_NOD1_N3_SP5_P1	1217	1243	572
BORG_NOD1_N5_SP1_P1	1830	1926	895
BORG_NOD3_N2_SP1_P1	1322	1070	597
BORG_NOD3_N2_SP1_P2	1818	1449	886

Table S4: Parameters used to make Fig. 4 in the main text. t_{min} and t_{min} are the minimum and maximum crystal residence time (kyr). d is estimated storage depth (km). d_{min} and d_{max} are minimum and maximum storage depths based on uncertainties. Moho is the depth to the base of the crust (km). Moho depths were obtained from compilations made by Mantle and Collins (*66*) and Plank and Langmuir (*67*). Uranium series based crystal residence times were obtained from the compilation made by Cooper and Kent (*8*). Crystal residence times were calculated by subtracting the eruption age from the crystal age.

Location	$\mathbf{t_{min}}$	$\mathbf{t_{max}}$	**d**	$\mathbf{d_{min}}$	$\mathbf{d_{max}}$	$\mathbf{SiO_2}$	**Moho**	**Label**	**References**
Aleutians	0	41.3	7.5	3	12	67.86	28	AL	(*68*)
Guadeloupe island: La Soufriere	26.6	43.2	4.5	3	6	56.40	28	GS	(*69, 70*)
Soufriere, St Lucia	15	134	4.5	3	6	58.95	23	SL	(*10, 70*)
Mt St Helens	0	48.3	8.5	5	12	60.96	42	MSH	(*71–74*)
Mt Hood	4.5	145	6	4	8	61.00	42	MH	(*8, 75, 76*)
S Sister	0	7.6	8.5	5	12	72.00	40.5	SS	(*73, 77*)
Parinacota	0	108	8.5	6	11	62.00	70	PA	(*78, 79*)
Puyehue-Cordon Caulle	0	17.7	10	6	15	65.70	32.5	PCC	(*80, 81*)
Quizapu	0.3	5.2	7	5	13	63.64	35	QU	(*82, 83*)
Krafla	0	8.8	12	6	18	49.76	20	KF	(*28*)
Laki	0	8	9	3	15	49.28	25	LK	(*27, 84*)
George Farm Center, Kenya	7	67	3	1	6	73.00	34	GFC	(*85, 86*)
Longonot Volcano, Kenya	0	6	3	1	6	62.00	34	LV	(*86, 87*)
Kaharoa, OVC, Taupo, NZ	0	263.3	7	2	12	77.59	27	KT	(*9, 88*)
Santorini	0	49	10.5	6	15	67.00	23	SA	(*89, 90*)
Borgarhraun	0.2	2.6	24	19.8	28.2	48.00	19	BO	(*11, 12*)
Kos Plateau	23	81	8	7	9	75.00	30	KP	(*91, 92*)
Soufriere, St Vincent	19	90	8.5	5	12	53.50	24	SV	(*93*)
Kilauea	0	1.3	5.5	2	9	51.13	13.5	KA	(*94, 95*)

Data S1. (Separate file)
Spreadsheet containing compositional data of spinel, plagioclase and glass used in this study. The spinel data is EPMA profile data which includes calculated mineral formulae for each point (using stochiometry). Ferric iron content was calculated using stochiometry. Standard deviations of spinel data are from counting statistics associated with each EPMA analysis. Greyscale values and spinel compositions used to calibrate the EDS maps of the Borgarhraun nodules are also included. The plagioclase data includes SIMS and EPMA profile analyses. All plagioclase elemental data is presented as parts per million (ppm). Standard deviations of each method used to obtain plagioclase data are also included. Glass data are EPMA analyses of Borgarhraun tephra glass and melt pockets adjacent to spinel crystals. Standard deviations for glass data are from counting statistics associated with each EPMA analysis.

Data S2. (Separate file)
Compiled database of spinel Cr-Al interdiffusion and Cr tracer diffusion experiments used to derive the multiple linear regression for the Cr-Al interdiffusion coefficient and associated covariance matrix used in this study. Experimental data is from Suzuki et al. (*24*) and Posner et al. (*25*).

Data S3. (Separate file)
Median values for all of the inverted parameters estimated for each spinel profile from the nested sampling Bayesian inversion. All of the Monte Carlo realisations for each model are also included in this file.

Data S4. (Separate file)
Parameters and associated statistics of the Cr-Al diffusion coefficient multivariate linear regression.

References

1. K. V. Cashman, R. S. J. Sparks, J. D. Blundy, *Science* **355**, eaag3055 (2017).
2. F. Costa, R. Dohmen, S. Chakraborty, *Reviews in Mineralogy and Geochemistry* **69**, 545 (2008).
3. K. M. Cooper, *Philosophical Transactions of the Royal Society A* **377**, 20180009 (2019).
4. K. Saunders, J. Blundy, R. Dohmen, K. Cashman, *Science* **336**, 1023 (2012).
5. P. Ruprecht, T. Plank, *Nature* **500**, 68 (2013).
6. T. H. Druitt, F. Costa, E. Deloule, M. Dungan, B. Scaillet, *Nature* **482**, 77 (2012).
7. E. J. F. Mutch, J. Maclennan, O. Shorttle, M. Edmonds, J. F. Rudge, *Nature Geoscience* **In press**, In press (2019).
8. K. M. Cooper, A. J. Kent, *Nature* **506**, 480 (2014).
9. A. E. Rubin, *et al.*, *Science* **356**, 1154 (2017).
10. M. Barboni, *et al.*, *Proceedings of the National Academy of Sciences* **113**, 13959 (2016).
11. J. Maclennan, *et al.*, *Geochemistry, Geophysics, Geosystems* **4** (2003).
12. B. Winpenny, J. Maclennan, *Journal of Petrology* **52**, 1791 (2011).
13. D. A. Neave, K. D. Putirka, *American Mineralogist* **102**, 777 (2017).
14. M. B. Holness, *et al.*, *Journal of Petrology* **48**, 1243 (2007).
15. K. M. Gillis, *et al.*, *Nature* **505**, 204 (2014).
16. J. Korenaga, P. B. Kelemen, *Journal of Geophysical Research: Solid Earth* **102**, 27729 (1997).
17. J. Maclennan, *Journal of Petrology* **49**, 1931 (2008).
18. J. Maclennan, D. McKenzie, F. Hilton, K. Gronvöld, N. Shimizu, *Journal of Geophysical Research: Solid Earth* **108** (2003).
19. K. Ozawa, *Nature* **338**, 141 (1989).
20. W. Meurer, M. Meurer, *Contributions to Mineralogy and Petrology* **151**, 187 (2006).
21. A. Thomson, J. Maclennan, *Journal of Petrology* **54**, 745 (2012).

22. M. Alnæs, *et al.*, *Archive of Numerical Software* **3**, 9 (2015).

23. F. Feroz, M. Hobson, M. Bridges, *Monthly Notices of the Royal Astronomical Society* **398**, 1601 (2009).

24. A. Suzuki, A. Yasuda, K. Ozawa, *Physics and Chemistry of Minerals* **35**, 433 (2008).

25. E. S. Posner, J. Ganguly, R. Hervig, *Geochimica et Cosmochimica Acta* **175**, 20 (2016).

26. O. Shorttle, *et al.*, *Earth and Planetary Science Letters* **427**, 272 (2015).

27. I. N. Bindeman, O. Sigmarsson, J. Eiler, *Earth and Planetary Science Letters* **245**, 245 (2006).

28. K. M. Cooper, K. W. Sims, J. M. Eiler, N. Banerjee, *Contributions to Mineralogy and Petrology* **171**, 54 (2016).

29. O. Jagoutz, M. W. Schmidt, *Chemical Geology* **298**, 79 (2012).

30. C. Stamper, J. Blundy, R. Arculus, E. Melekhova, *Journal of Petrology* **55**, 1353 (2014).

31. T. Parsons, *et al.*, *Geology* **26**, 199 (1998).

32. K. Sims, *et al.*, *Geochimica et Cosmochimica Acta* **63**, 4119 (1999).

33. M. C. Humphreys, S. L. Kearns, J. D. Blundy, *American Mineralogist* **91**, 667 (2006).

34. J. Schindelin, *et al.*, *Nature methods* **9**, 676 (2012).

35. T. J. Holland, E. C. Green, R. Powell, *Journal of Petrology* **59**, 881 (2018).

36. I. A. Sigurdsson, S. Steinthorsson, K. Grönvold, *Earth and Planetary Science Letters* **183**, 15 (2000).

37. J. Maclennan, *Philosophical Transactions of the Royal Society A* **377**, 20180021 (2019).

38. H.-J. Yang, R. J. Kinzler, T. Grove, *Contributions to Mineralogy and Petrology* **124**, 1 (1996).

39. V. C. Kress, I. S. Carmichael, *Contributions to Mineralogy and Petrology* **108**, 82 (1991).

40. M. S. Ghiorso, R. O. Sack, *Contributions to Mineralogy and Petrology* **119**, 197 (1995).

41. G. A. Gualda, M. S. Ghiorso, R. V. Lemons, T. L. Carley, *Journal of Petrology* **53**, 875 (2012).

42. J. Crank, *The mathematics of diffusion* (Oxford university press, 1979).

43. F. Feroz, M. Hobson, E. Cameron, A. Pettitt, *arXiv preprint arXiv:1306.2144* (2013).

44. J. Buchner, *et al.*, *Astronomy & Astrophysics* **564**, A125 (2014).

45. C. Geuzaine, J.-F. Remacle, *International journal for numerical methods in engineering* **79**, 1309 (2009).

46. The CGAL Project, *CGAL User and Reference Manual* (CGAL Editorial Board, 2018), 4.12.1 edn.

47. B. Winpenny, J. Maclennan, *Journal of Petrology* **55**, 2537 (2014).

48. R. L. Nielsen, *et al.*, *Geochemistry, Geophysics, Geosystems* **18**, 3359 (2017).

49. K. Faak, S. Chakraborty, L. A. Coogan, *Geochimica et Cosmochimica Acta* **123**, 195 (2013).

50. J. A. Van Orman, D. J. Cherniak, N. T. Kita, *Earth and Planetary Science Letters* **385**, 79 (2014).

51. D. J. Cherniak, E. B. Watson, *Geochimica et Cosmochimica Acta* **58**, 5179 (1994).

52. B. Giletti, J. Casserly, *Geochimica et Cosmochimica Acta* **58**, 3785 (1994).

53. D. Cherniak, *Geochimica et Cosmochimica Acta* **66**, 1641 (2002).

54. L. V. Danyushevsky, P. Plechov, *Geochemistry, Geophysics, Geosystems* **12** (2011).

55. M. B. Holness, *Contributions to Mineralogy and Petrology* **168**, 1076 (2014).

56. P. L. Roeder, A. Poustovetov, N. Oskarsson, *The Canadian Mineralogist* **39**, 397 (2001).

57. S. Matthews, O. Shorttle, J. Maclennan, *Geochemistry, Geophysics, Geosystems* **17**, 4725 (2016).

58. M. B. Holness, M. J. Cheadle, D. McKenzie, *Journal of Petrology* **46**, 1565 (2005).

59. M. B. Holness, T. F. Nielsen, C. Tegner, *Journal of Petrology* **48**, 141 (2006).

60. J. Leuthold, J. Blundy, M. Holness, R. Sides, *Contributions to Mineralogy and Petrology* **168**, 1021 (2014).

61. C. J. Lissenberg, C. J. MacLeod, K. A. Howard, M. Godard, *Earth and Planetary Science Letters* **361**, 436 (2013).

62. V. Stubican, J. Osenbach, *Advances in Ceramics* **10**, 406 (1984).

63. T. Sugawara, *Journal of Geophysical Research: Solid Earth* **105**, 8457 (2000).

64. I. N. Bindeman, A. M. Davis, M. J. Drake, *Geochimica et Cosmochimica Acta* **62**, 1175 (1998).

65. R. Dohmen, J. Blundy, *American Journal of Science* **314**, 1319 (2014).

66. G. Mantle, W. Collins, *Geology* **36**, 87 (2008).

67. T. Plank, C. H. Langmuir, *Earth and Planetary Science Letters* **90**, 349 (1988).

68. B. R. Jicha, B. S. Singer, B. L. Beard, C. M. Johnson, *Earth and Planetary Science Letters* **236**, 195 (2005).

69. M. Touboul, B. Bourdon, B. Villemant, G. Boudon, J.-L. Joron, *Chemical Geology* **246**, 181 (2007).

70. C. Annen, M. Pichavant, O. Bachmann, A. Burgisser, *Journal of Geophysical Research: Solid Earth* **113** (2008).

71. K. M. Cooper, M. R. Reid, *Earth and Planetary Science Letters* **213**, 149 (2003).

72. L. L. Claiborne, C. F. Miller, D. M. Flanagan, M. A. Clynne, J. L. Wooden, *Geology* **38**, 1011 (2010).

73. J. Gardner, M. Rutherford, S. Carey, H. Sigurdsson, *Bulletin of Volcanology* **57**, 1 (1995).

74. J. S. Pallister, *et al.*, Petrology of the 2004-2006 Mount St. Helens lava dome–implications for magmatic plumbing and eruption triggering: Chapter 30 in A volcano rekindled: the renewed eruption of Mount St. Helens, 2004-2006, *Tech. rep.*, US Geological Survey (2008).

75. G. R. Eppich, K. M. Cooper, A. J. Kent, A. Koleszar, *Earth and Planetary Science Letters* **317**, 319 (2012).

76. A. M. Koleszar, A. J. Kent, P. J. Wallace, W. E. Scott, *Journal of Volcanology and Geothermal Research* **219**, 1 (2012).

77. M. E. Stelten, K. M. Cooper, *Earth and Planetary Science Letters* **313**, 1 (2012).

78. B. Bourdon, G. Wörner, A. Zindler, *Contributions to Mineralogy and Petrology* **139**, 458 (2000).

79. M. Banaszak, Differentiation regimes in the Central Andean magma systems: case studies of Taapaca and Parinacota volcanoes, Northern Chile, Ph.D. thesis, Niedersächsische Staats-und Universitätsbibliothek Göttingen (2014).

80. B. R. Jicha, *et al.*, *Earth and Planetary Science Letters* **255**, 229 (2007).

81. D. C. Gerlach, F. A. Frey, H. Moreno-Roa, L. Lopez-Escobar, *Journal of Petrology* **29**, 333 (1988).

82. P. Ruprecht, G. W. Bergantz, K. M. Cooper, W. Hildreth, *Journal of Petrology* **53**, 801 (2012).

83. P. Ruprecht, K. M. Cooper, *Journal of Petrology* **53**, 841 (2012).

84. D. A. Neave, E. Passmore, J. Maclennan, G. Fitton, T. Thordarson, *Journal of Petrology* **54**, 1661 (2013).

85. A. Heumann, G. R. Davies, *Journal of Petrology* **43**, 557 (2002).

86. L. Field, J. Blundy, R. Brooker, T. Wright, G. Yirgu, *Bulletin of Volcanology* **74**, 981 (2012).

87. N. W. Rogers, P. J. Evans, S. Blake, S. C. Scott, C. J. Hawkesworth, *Journal of Petrology* **45**, 1747 (2004).

88. G. A. Gualda, *et al.*, *Science advances* **4**, eaap7567 (2018).

89. G. Zellmer, S. Turner, C. Hawkesworth, *Earth and Planetary Science Letters* **174**, 265 (2000).

90. A. Cadoux, B. Scaillet, T. H. Druitt, E. Deloule, *Journal of Petrology* **55**, 1129 (2014).

91. O. Bachmann, B. Charlier, J. Lowenstern, *Geology* **35**, 73 (2007).

92. J. Keller, *Bulletin Volcanologique* **33**, 942 (1969).

93. E. Heath, S. P. Turner, R. Macdonald, C. J. Hawkesworth, P. Van Calsteren, *Earth and Planetary Science Letters* **160**, 49 (1998).

94. K. M. Cooper, M. R. Reid, M. T. Murrell, D. A. Clague, *Earth and Planetary Science Letters* **184**, 703 (2001).

95. P. T. Delaney, R. S. Fiske, A. Miklius, A. T. Okamura, M. K. Sako, *Science* **247**, 1311 (1990).